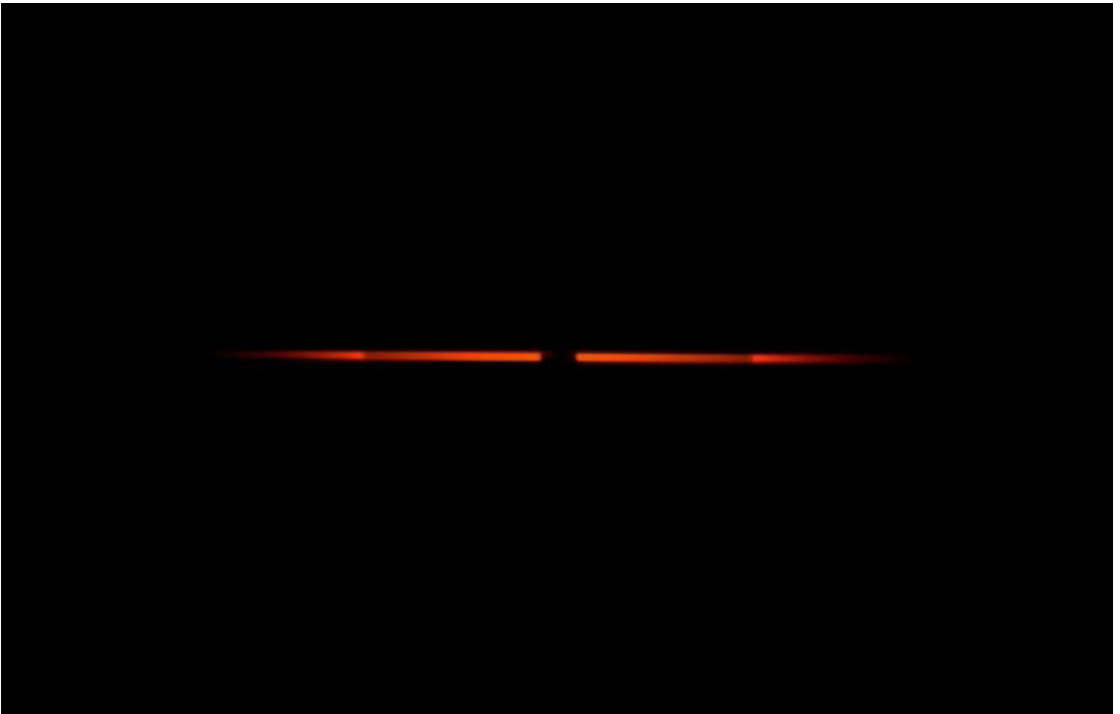Doctoral Thesis in Physics

Temperature measurements on silicon core optical fibers during CO₂ laser processing

KORBINIAN MÜHLBERGER

Temperature measurements on silicon core optical fibers during CO₂ laser processing

KORBINIAN MÜHLBERGER

Cover page photo: Molten core of a silicon core fiber

"Des is wia bei jeda Wissenschaft, am Schluss stellt sich dann heraus,
dass alles ganz anders war."
— Karl Valentin

Abstract

This thesis presents temperature measurements on silicon core optical fibers during CO_2 laser processing. Silicon core fibers are a new type of fiber offering a unique platform to combine the optoelectronic properties of silicon and the possibilities of the optical fiber platform. This makes them a promising candidate for many applications, such as mid-IR detection and transmission, studies of nonlinear optical devices, or fiber amplifiers. Today, two hurdles limit their usage: high optical transmission losses and complicated coupling into the core due to its high refractive index.

The first task of this thesis work was to find suitable postprocessing of the as-drawn fibers in order to decrease optical transmission losses. The goal was to improve the fibers by the liquid-phase recrystallization method. In this method, the core of the fiber is heated to a temperature above its melting point by a laser beam. By scanning the beam along the fiber, a melt zone is moved through the fiber. When the silicon solidifies, it recrystallizes into a single crystal with lower optical losses. Successively, a fully computer-controlled setup was developed for fiber processing. Furthermore, a lab-size fiber draw tower was built to fabricate specialty fibers, especially silicon core fibers. Here, a CO laser acts as the heat source. The developed draw tower is very flexible and can be used to manufacture ample amounts of many fiber types, suitable for rapid prototyping.

It is known that the cooling rate at which the silicon core solidifies is a crucial parameter for the final transmission losses. Yet, it has so far only been estimated from black-body radiation. Here, an interferometric method was developed, allowing for in-situ temperature measurements in silicon core optical fibers. The method relies on probing the fiber with a laser beam during processing and observing the interference pattern caused by glass reflections. A suitable calibration of the interference pattern with temperature allowed to remotely monitor the fiber temperature in real-time during processing with high precision.

Sammanfattning

I denna avhandling presenteras temperaturmätningar på optiska fibrer med kiselkärnor när de bearbetas med en CO_2 laser. Kiselkärnfibrer är en ny typ av optiska fiber som erbjuder en unik platform att kombinera optoelektroniska egenskaper hos kisel och fiberformatets geometri. Detta gör dem till en lovande kandidat för många olika tilllämpningar, detektion och transmission av mid-IR, studier av icke-linjära optiska effekter eller som fiberförstärkare. Idag finns det två begränsningar för deras användning: höga optiska transmissionsförluster och komplicerad inkoppling på grund av det höga brytningsindexet för kärnan.

Den första uppgiften i denna avhandling var att finna en lämplig efterbehandling av den tillverkade fibern för att minimera optiska transmissionsförluster. Tanken var att förbättra fibrerna genom att smälta kärnan och låta den omkristallisera och bilda en singelkristall. Med den utvecklade metoden värms fiberns kärna till en temperatur över sin smältpunkt av en laserstråle. När strålen skannas längs fibern flyttas en smältzon genom fibern. Bakom smältzonen omkristalliseras kislet och en lång singelkristall bildas med lägre optiska förluster. Succesivt utvecklades metoden till att bli helt datorstyrd vilket gav fibrer med de lägsta förluster som hittills uppnåtts. I en andra fas byggdes ett fiberdragtorn i labbstorlek för att tillverka fibrer med specialkärnor, speciellt halvledarkärnor. Här användes en CO laser som värmekälla för att tillverka fibern. Denna metod är mycket flexibel och kan användas för snabb protoyp tillverkning av många olika typer av fibrer.

Även om det är känt att avkylningshastigheten med vilken kiselkärnan stelnar är en avgörande parameter för de slutliga transmissionsförlusterna, har den hittills endast uppskattats från svartkroppsstrålning. I nästa fas utvecklades en interferometrisk metod som möjliggör in-situ temperaturmätningar av optiska fibrer (med kiselkärna) under själva processningen. Metoden bygger på att belysa fibern med en laserstråle medan den bearbetas och observera det uppkomna interferensmönstret från reflexer i glaset. En kalibrering av interferensmönstret mot temperaturen gjorde det möjligt att fjärrövervaka fibertemperaturen i realtid under bearbetningen med hög noggrannhet.

Preface

The research presented in this thesis was carried out within the Laser Physics group at the Department of Applied Physics of the Royal Institute of Technology (KTH) in Stockholm, Sweden.

List of publications

Paper I

K. Mühlberger, C. M. Harvey, and M. Fokine, "In-situ non-contact high-temperature measurement of an optical fiber up to the glass softening point", *Optics Express* **29**, 7825–7832 (2021).

Paper II

K. Mühlberger, C. M. Harvey, and M. Fokine, "High-performance arduino-based interferometric quadrature phase-shift detection system with 1 nm resolution", *AIP Advances* **11**, 105304 (2021).

Paper III

C. M. Harvey, K. Mühlberger, T. Oriekhov, P. Maniewski, and M. Fokine, "Specialty optical fiber fabrication: fiber draw tower based on a CO laser furnace", *Journal of the Optical Society of America B* **38**, F122-F129 (2021).

Paper IV

C. M. Harvey, K. Mühlberger, and M. Fokine, "Mach-Zehnder Interferometer for In-Situ Non-Contact Temperature Monitoring During Thermal Processing of an Optical Fibre", *Journal of Lightwave Technology* **39**, 7223-7230 (2021).

Paper V

K. Mühlberger, C. M. Harvey, and M. Fokine, "Temperature dynamics in silicon core fibers during CO_2 laser processing", *Optics Express* **30**, 92-100 (2022).

Author contributions

Paper I

I conducted the experiments, performed data analysis, and co-wrote the manuscript.

Paper II

I built the experimental setup, conducted the experiments, performed data analysis, and co-wrote the manuscript.

Paper III

I drafted the code to operate the fiber draw tower, contributed actively to the development of the draw tower, and co-wrote the manuscript.

Paper IV

I contributed to the design and building of the experimental setup, performed parts of the data analysis, and co-wrote the manuscript.

Paper V

I designed and built the experimental setup, performed the data analysis, discussed the results, and co-wrote the manuscript.

Additional publications

- W. Wu, M. H. Balci, K. Mühlberger, M. Fokine, F. Laurell, T. Hawkins, J. Ballato, and U. J. Gibson, "Ge-capped SiGe core optical fibers", *Optical Materials Express* **9**, 4301-4306 (2019).

- T. Oriekhov, C. M. Harvey, K. Mühlberger, and M. Fokine, "Specialty optical fiber fabrication: preform manufacturing based on asymmetrical CO Laser heating", *Journal of the Optical Society of America B* **38**, 130-137 (2021).

Conference contributions

- M. Fokine, K. Mühlberger, T. Oriekhov, S. Tjörnhammer, F. Laurell, and U. J. Gibson, "Laser processing of semiconductor core fibers", *XL Encontro Nacional de Física da Matéria Condensada*, Búzios, Brazil, ID: 44–1 [02.4] (2017).

- K. Mühlberger, T. Oriekhov, M. Fokine, F. Laurell, and U. J. Gibson, "Processing of semiconductor core fibers with CO_2 laser beam irradiation", *Optics & Photonics in Sweden*, Stockholm, Sweden (2017).

- T. Sørgård, K. Mühlberger, W. Wu, X. Yang, T. Hawkins, J. Ballato, F. Laurell, M. Fokine, and U. J. Gibson, "Reduced loss in SiGe-core optical fibers", *Conference on Lasers and Electro-Optics*, San Jose, USA, SF3I.6 (2018).

- K. Mühlberger, F. Laurell, U. J. Gibson, and M. Fokine, "CO_2 laser beam characterization by using a fiber Bragg grating", *Northern Optics & Photonics*, Lund, Sweden (2018).

- K. Mühlberger, T. Oriekhov, F. Laurell, U. J. Gibson, and M. Fokine, "Postprocessing of semiconductor-core fibers", *Optics & Photonics in Sweden*, Stockhom, Sweden (2019).

- K. Mühlberger, C. M. Harvey, and M. Fokine, "In-situ Non-contact High-temperature Measurement of an Optical Fiber up to the Glass Softening Point", *Optical Sensors and Sensing Congress*, Vancouver, Canada, STu4D.3 (2020).

- C. M. Harvey, K. Mühlberger, and M. Fokine, "Non-contact Interferometric Technique for Fabrication of Silica Microspheres with Improved Ellipticity", *Optical Sensors and Sensing Congress*, Vancouver, Canada, SM1B.7 (2020).

- K. Mühlberger, C. M. Harvey, and M. Fokine, "Temperature Dynamics in Silicon Core Fibers during CO_2-Laser Processing", *Conference on Lasers and Electro-Optics Europe and European Quantum Electronics Conference*, Munich, Germany, CE–7.6 (2021).

- C. M. Harvey, K. Mühlberger, T. Oriekhov, and M. Fokine, "CO laser-based furnace for optical fibre fabrication", 4th *International Conference on Optics, Photonics and Lasers*, Corfu, Greece (2021).

- C. M. Harvey, K. Mühlberger, T. Oriekhov, and M. Fokine, "Low-loss Silicon-core Optical Fibre Fabrication Using a CO Laser-based Furnace without an Interface Layer", *Frontiers in Optics + Laser Science*, Washington D.C., USA, FW1C.2 (2021).

Acknowledgments

The presented thesis is the result of an insightful journey and a lot of hard work in the past five years. It would not have been possible without the help and support of countless people, for which I am deeply grateful.

First of all, I would like to thank Prof. Fredrik Laurell for accepting me into the Laser Physics Group and for the help and guidance throughout the entire time. I would also like to express my gratitude to Prof. Ursula Gibson, for providing me with precious fiber and advising me during my first research baby steps.

Research, as I learned over time, while often being the best imaginable playground can be quite frustrating at other times. I was fortunate enough to be on this journey with colleagues who shared my headaches and made every day a lot more enjoyable.

One of my highlights was a research stay in Brazil that would not have been possible without Prof. Anderson Gomes and Prof. Isabel C. S. Carvalho, who also prevented me from getting injured by psoralen and UV radiation.

There is more to life than work. I am greatful for my amazing friends and a very understanding family tolerating me and supporting me throughout this endeavor.

Finally, I want to thank Prof. Michael Fokine for supervising me growing up in the lab. I was listening more than once to advice that, only after I made some mistake or set parts on fire, was able to fully understand and realize my obstacles were foreseen. Yet, I was given the freedom to explore and make all those mistakes myself. Additionally, I really got inspired to have a more detailed look at results, to think further and explore, and to make up ideas for consecutive experiments. In countless discussions, I also learned how to structure my thoughts when I got stuck. But most of all I am grateful, that besides all the work stuff, I felt welcome at KTH from day one.

Contents

1 Introduction

Semiconductor core fibers are the attempt to combine two technologies that had arguably an huge impact on everyday life. One technology is the optical fiber [1], the workhorse of modern communication and an irreplaceable tool in fundamental research. The other is semiconductors on insulators which are the core of all electronic devices used today. Although the idea of filling glass tubes with metals and drawing them into fiber has been around since at least 1924 [2], the first semiconductor core fiber was only demonstrated recently, in 2006 [3]. Therefore, Section 1.1 intends to highlight why semiconductor core fibers are such an interesting hybrid platform to investigate.

The initial direction of this thesis was to explore possible ways to reduce optical transmission losses of semiconductor core fibers. The focus lay on the liquid-phase recrystallization method [4] generally known as zone melting [5]. Progressively the focus of the thesis became non-contact in-situ high-temperature measurements on optical fibers, both all-silica glass and silicon-core silica-clad fibers, as well as their fabrication. This evolution is outlined in Section 1.2.

1.1 Semiconductor core fibers

Although all-silica fibers are produced at very low costs and enable the high-speed communication we are used to today, their application is limited due to their transmission window being restricted to wavelengths below approximately $2.5\,\mu\text{m}$ [6]. There are various approaches to access transmission windows beyond $2.5\,\mu\text{m}$, for example, by microstructuring optical fibers [7] or by using different materials such as chalcogenide glasses [8, 9]. Another approach is to put elemental (Si, Ge) or compound (e.g. ZnSe, InSb) semiconductors in the core of a silica-clad fiber and thereby extend the transmission window far into

the infrared [10, 11]. Semiconductor core fibers promise not only to be a unique platform for THz-transmission [12] and mid-IR sensing, but also for nonlinear optical devices [13, 14] and fiber amplifiers due to their high nonlinear coefficients compared to silica [15]. Furthermore, semiconductors are the foundation of all modern electronic technologies. Ideally, semiconductor core fibers will combine the advantages of the glass fiber geometry, such as robustness, durability, and flexibility, with the exceptional optoelectronic properties of semiconductors [16, 17].

Semiconductor core fibers are usually either fabricated by high-pressure chemical vapor deposition (HPCVD) [18] or the molten core drawing technique (MCD) [19]. Both have advantages and disadvantages [15]. In short, HPCVD produces high purity fibers and enables a wide range of core materials, but the fiber length is limited to a few meters, and deposition rates are slow. The MCD is done in setups similar to conventional draw towers [19]. The preform is heated to a temperature above the melting point of the semiconductor. The glass cladding that encapsulates the core acts as the crucible during drawing. While this limits the range of possible materials, one significant advantage is that long lengths, i.e. hundreds of meters, can be produced at once. It is worth noting that the fibers are drawn at speeds of several meters per minute [20] and their semiconductor core is typically polycrystalline [4, 19, 21].

If semiconductor core fibers embody all those possibilities, why are they not already on all shelves? The reason are two main limitations that hinder practical applications of semiconductor core fibers today. One is the low coupling efficiency due to the relatively high refractive index of the semiconductor core ($n \geq 2$). Attempts have been made to overcome this by tapering a silicon core fiber, essentially creating a silicon nano-spike. Subsequent splicing to a single-mode fiber (SMF) showed coupling losses of $4\,\mathrm{dB}$, and this is theoretically expected to be even below $1\,\mathrm{dB}$ [22]. This loss, like all other losses described in the following text, was measured in the near-infrared, where semiconductor core fibers are usually characterized due to the availability of light sources and detectors. The other limitation is the transmission loss typically exceeding $1\,\mathrm{dB\,cm^{-1}}$, which makes guiding light over more than a meter complicated. One likely reason

is contamination of the core by oxygen diffusion during the MCD [21]. This has been addressed by reducing heating times [20] or introducing interface layers between core and cladding [23]. Another approach to tackle the high as-drawn losses is suitable postprocessing which has been a necessary fabrication step to reduce optical transmission losses [24]. The postprocessing usually entails either direct heating of the core by an argon ion laser [25] or heating the silica-cladding by a CO_2 laser [26]. In both cases, the core is heated above its melting point. The laser is then scanned along the fiber. When the fiber cools down, it recrystallizes into a single crystal and optical transmission losses drop [25, 26]. Recently, it has also been shown that by using a sophisticatedly structured preform as-drawn fiber losses can be as low as $0.2 \, \mathrm{dB \, cm^{-1}}$ [27]. This loss value is already comparable to the silicon-on-insulator platform [28]. It is, however, drastically above loss values measured in the bulk of approximately $0.000 \, 02 \, \mathrm{dB \, cm^{-1}}$ [29]. The high losses of semiconductor core fibers today seem to constitute a solvable problem if one dares to estimate a plausible development similar to that of all-glass optical fibers, where losses have been reduced from several hundreds of $\mathrm{dB \, km^{-1}}$ [1] to less than $20 \, \mathrm{dB \, km^{-1}}$ [30] and commercially available fiber today has losses well below $1 \, \mathrm{dB \, km^{-1}}$.

1.2 Evolution of the thesis

The initial aim of this thesis was to explore the liquid-phase recrystallization method [4] of semiconductor core fibers to reduce the optical transmission losses of as-drawn fibers [26]. Using this method, the semiconductor core of the fiber is molten and recrystallized into a single crystal by scanning the beam of a CO_2 laser along with the fiber. Hence, a sophisticated CO_2 laser processing setup was developed initially. Later, an additional focus became silicon core fiber fabrication and optical metrology to measure the temperature dynamics in semiconductor core fibers during postprocessing. Since all work was done on silicon core fibers (SCFs), the following discussion is restricted to silicon as a core material. However, the presented techniques apply to other semiconductor core materials as well.

The initial laser processing experiments of SCFs indicated that the heating power provided by the CO_2 laser was not sufficiently stable. To

counter this instability, foremost good monitoring of the laser-induced heat in silica was needed. The development of such a monitoring system led to **Paper I**. The data collection and real-time processing to get direct feedback from heat monitoring was done by a setup built around a microcontroller. Its working principle and capabilities are described in **Paper II**. This microcontroller was extended into an entire control system for the fiber processing setup, explained in detail in Chapter 3. Concurrently, a fiber draw tower was developed centered around the manufacture of SCFs. The developed tower was successfully used for fabricating a wide range of fibers and ensured a sufficient supply of SCFs. The function principle of the tower and initially drawn fibers are presented in **Paper III**. Both the fiber draw tower and the laser processing system are computer-controlled by self-written *Python* software. It provides full control over all parts of the two systems and provides a graphical user interface. With the working fiber processing setup and ample SCFs, the processing could start. One critical unknown parameter during fiber processing was the temperature, which has so far only been estimated from thermal emission. The temperature measurement technique used to monitor the CO_2 laser power would be applicable for SCFs, yet incurs complications in choice of wavelength and data processing due to the drastically different refractive indices and absorption coefficients of silicon and silica. An alternative interferometric approach to measure temperature in fibers with an opaque core was designed and is highlighted in **Paper IV**. This technique was applied to add one puzzle piece of knowledge about SCF processing. It was finally possible to determine the temperature in SCFs during laser processing. This technique is presented in the final **Paper V**.

2 Interferometry in the cross-section of optical fibers

In the scope of this thesis, the circular geometry of the optical fiber cross-section was used as a cavity for two types of interferometers to perform in-situ temperature measurements on the optical fiber itself. This chapter covers a quick introduction to the possible interferometer geometries in optical fibers and an explanation of how the temperature of the fiber can be obtained by monitoring the phase change in the interference pattern of those interferometers. This is the metrological foundation for the appended **Paper I, II, IV and V**.

2.1 Interferometer configurations

Light scattering from cavities with a circular symmetry can be described by a mathematical series introduced by Debye in 1908 [31] for incident light with a wavelength that is small compared to the radius of the cavity. Geometrical optics can then describe the light scattering from such cavities, i.e., it is sufficient to consider Fresnel reflections at the interfaces between the ambient refractive index and the refractive index of the cavity. A general case for light scattering at a circular cavity is shown in Fig. 2.1.

The incident beam is partially reflected at the surface of the cavity, and this partial reflection is the first Debye mode labeled p_0. The part of the incident beam that is refracted into the cavity and then leaves the cavity on the other side is the second Debye mode labeled p_1. This can be done iteratively to describe all possible combinations of reflected and refracted beams by p_i with $i \in \mathbb{N}$. An incident collimated beam with a diameter equal or greater than the cavity would result in interference among all different scattering modes making the interpretation of the interference pattern more complex.
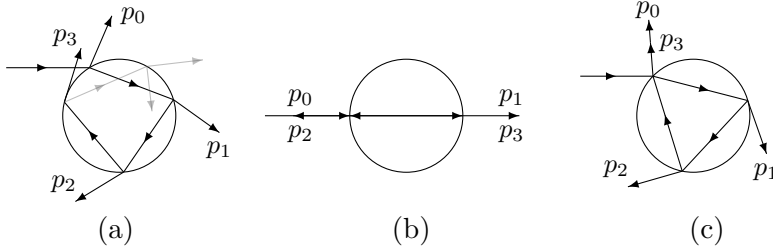
Figure 2.1: Sketches of light scattering at a circular cavity showing the first Debye modes for (a) the general case, (b) the Fabry-Pérot type configuration and (c) the Mach-Zehnder type configuration.

This can be prevented by using a focused laser beam limiting the angular distribution of scattering modes. This allows for a higher degree of selection of the desired different scattering modes close to the sketch in Fig. 2.1.

Generally, it can be said that the beam path inside the cavity and its overlap with the incoming laser beam depends on the refractive index and the dimension of the cavity, as well as the incident angle and the wavelength of the laser beam. Careful alignment of a laser beam with respect to the cavity allows for different Debye modes of scattering to be co-aligned and overlap. The modes can interfere at a position outside the cavity, as shown in Fig. 2.1(b) for a Fabry-Pérot type interferometer (FPI) and in Fig. 2.1(c) for a Mach-Zehnder type interferometer (MZI). A detailed description of the original Fabry-Pérot and Mach-Zehnder interferometer can be found in Ref. [32]. In both cases, FPI and MZI, the recombined beams will interfere and produce an interference pattern. The exact appearance of this interference pattern depends on the phase difference of the two beams, that is, how much phase the beam inside the cavity gained with respect to the Debye mode p_0. How much the phase ϕ advances depends on the optical path length (OPL), which depends on temperature T. The phase is given by

$$\phi\left(T\right) = \frac{2\pi}{\lambda} \cdot n\left(T\right) \cdot L\left(T\right), \tag{2.1}$$

where λ is the wavelength of the incident light, n is the refractive index of the cavity and L is the geometrical length of the beam path

inside the cavity. The refractive index and the physical dimension of the cavity are dependent on temperature coupled through the thermo-optic coefficient and thermal expansion coefficient, respectively. How measuring the temperature-dependent phase can be used to obtain the temperature of the cavity is described in the following sections.

The discussion is limited to a circular fused silica cavity, i.e., the cross-section of an optical fiber, probed by a HeNe laser operating at a wavelength of $\lambda = 632.8\,\text{nm}$. In this case, the FPI and the MZI are the only two possibilities for the interference of Debye modes. This follows from a simple consideration: $m \in \mathbb{N}$ internal reflections form a geometric figure inside the cavity having m corners. The sum of all inner angles α of the figure is given by $\sum \alpha = (m - 2) \cdot \pi$. Since inside the cavity the incident angle α_0 and the angle of reflection α_r are identical, it follows that $(m - 2) \cdot \pi = 2m \cdot \alpha_r$. Thus, for more than three internal reflections the angle of reflection has to be $\alpha_r > \frac{\pi}{4}$. This angle is already larger than the critical angle so light can't leave the cavity due to total internal reflection.
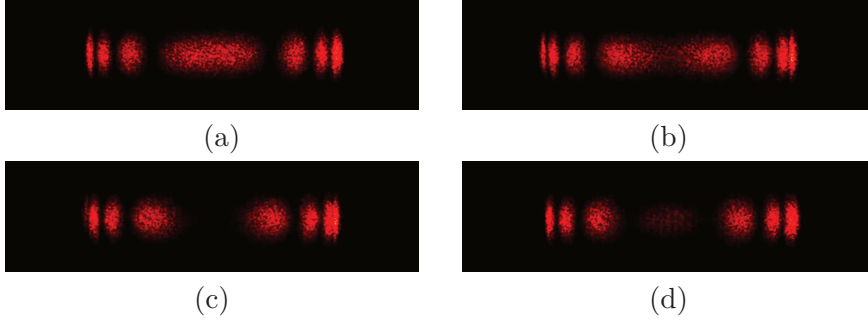
2.1.1 Fabry-Pérot type interferometer

The simplest interferometer design in the cross-section of an optical fiber is the FPI as illustrated in Fig. 2.2. A laser beam is axially
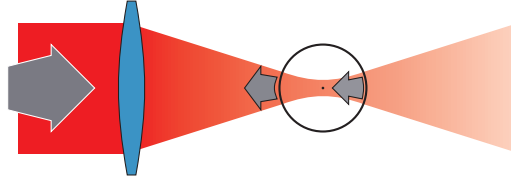
Figure 2.2: Schematic of the Fabry-Pérot-type interferometer illustrating the Fresnel reflections from the two opposite surfaces of the optical fiber.

focused onto the fiber, which is positioned such that the surface is close to the focal point of the laser beam. There are two main Fresnel reflections originating from the front and back surface of the fiber. The back-scattered light overlaps and causes an interference pattern that typically looks like the photographs shown in Fig. 2.3. The appearance

(a)

(b)

(c)

(d)

Figure 2.3: Typical interference patterns of a Fabry-Pérot type interferometer with increasing optical path length from (a) to (d).

of the interference pattern changes depending on the exact OPL. An increase of the OPL causes the fringes of the interference pattern to move outwards. Vice versa, a decrease in the OPL causes the fringes to move inwards. Thus, by monitoring the interference pattern, it is possible to extract information about changes in the phase of the beam entering the cavity and therefore changes in temperature of the cavity. The method to obtain the temperature from the phase is thoroughly discussed in Sections 2.2 and 2.3.

The dependence of the interference pattern on the phase can be described mathematically considering only Fresnel reflections. In the case of the FPI, there are two types of reflections that have to be considered. One from the front surface of the fiber, an air-to-glass interface, and one from the back surface, a glass-to-air interface, as sketched in Fig. 2.4. The initial beam $\vec{E}_i$ is partially reflected at the front surface $\vec{E}_r = r\vec{E}_i$. The part that is transmitted into the cavity $\vec{E}_t = t\vec{E}_i = \vec{E}_i'$ is again partially reflected $\vec{E}_r' = r'\vec{E}_i'$ and transmitted $\vec{E}_t' = t'\vec{E}_i'$ at the back surface. Thus the total field of the reflected laser beam $\vec{E}_{r,\text{total}}$ can be written as a sum of all partial contributions and is given by

$$\vec{E}_{r,\text{total}} = \vec{E}_i \left[r + tt'r'e^{i\phi} \left(1 + r'^2 e^{i\phi} + r'^4 e^{i2\phi} + \cdots \right) \right], \qquad (2.2)$$

where r, r' and t, t' are the amplitude coefficients for reflection and transmission at the air-glass and glass-air interface respectively and ϕ is the temperature dependent additional phase from one round-trip
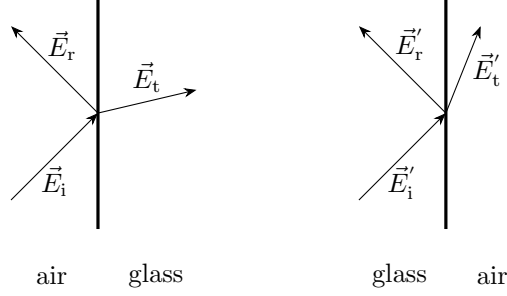
Figure 2.4: Sketch of the two possible Fresnel reflections in an optical fiber. The subscripts i, r, and t of the electric field vectors refer to the incident, reflected, and transmitted beam, respectively.

in the cavity. Using the Stokes relations ($r' = -r$, $r^2 + tt' = 1$) and the geometrical series, Eq. (2.2) simplifies to

$$\vec{E}_{r,\text{total}} = \vec{E}_i \left[\frac{r - re^{i\phi}}{1 - r^2 e^{i\phi}} \right]. \tag{2.3}$$

The intensity response function of the reflected light is given by

$$I\left(\phi\right) = \left| \frac{\vec{E}_{r,\text{total}}}{\vec{E}_i} \right|^2 \cdot I_0, \tag{2.4}$$

where I_0 is the initial light intensity. By combining Eq. (2.3) and Eq. (2.4), the intensity response function for the FPI can be written as

$$I\left(\phi\right) = \frac{2r^2 \left[1 - \cos\left(\phi\right)\right]}{1 + r^4 - 2r^2 \cos\left(\phi\right)} \cdot I_0. \tag{2.5}$$

This function is plotted in Fig. 2.5 for amplitude reflection coefficients $r \in [0, 0.5]$. For the air-silica interface at the incident angle of 0°, the reflection coefficient is $r = \pm 0.198$ indicated by the white dotted line. In this case, the intensity response function is well fitted by the sinusoidal function

$$I\left(\phi\right) = A_{\text{FP}} \left[1 - \cos\left(\phi\right)\right], \tag{2.6}$$

where $A_{\text{FP}} = 0.077 \cdot I_0$ is a fitting parameter obtained from Fig. 2.6 with an R^2-value of 0.997.
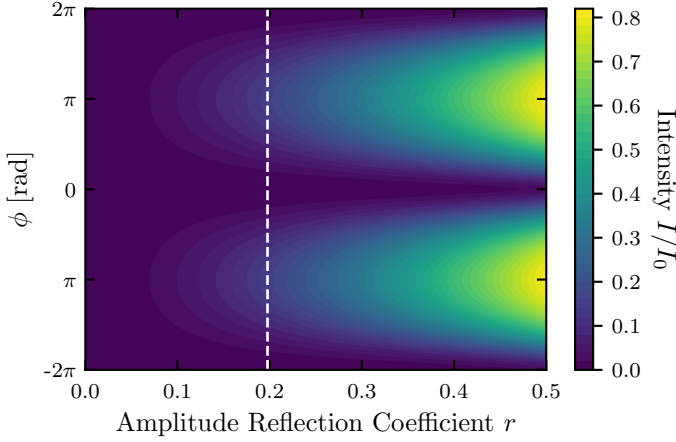
Figure 2.5: Contour plot of the intensity response function for a Fabry-Pérot type interferometer. The white dotted line indicates the amplitude reflection coefficient $r = 0.198$.

2.1.2 Mach-Zehnder type interferometer

Instead of aligning the incident laser beam perpendicular to the fiber surface, it is also possible to probe the fiber at an angle as sketched in Fig. 2.1(c). At the correct incident angle $\alpha_0 = 46.8°$, a MZI is formed and p_0 overlaps with p_3. The total electric field of the reflected light is obtained analogously to the Fabry-Pérot case
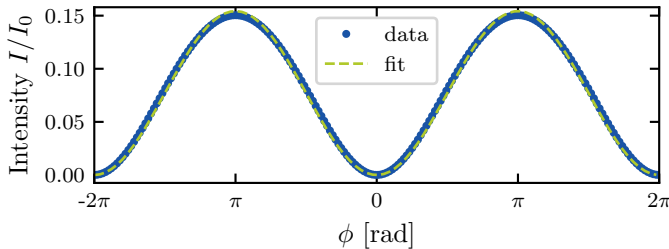
Figure 2.6: Slice of the intensity response function of the Fabry-Pérot type interferometer at $r = 0.198$ fitted by a sinusoid.

described in Section 2.1.1 and is given by

$$\vec{E}_{\mathrm{r,total}} = \vec{E}_{\mathrm{i}} \left[\frac{r + r^2 e^{i\phi}}{1 + r^3 e^{i\phi}} \right], \tag{2.7}$$

where ϕ is the phase for one round trip in the cavity. In contrast to the FPI case, the amplitude reflection coefficients $r_\parallel, r_\perp$ for in- and out-of-plane polarized light differ in the MZI. The total intensity response function is still calculated using Eq. (2.4), but $I_\parallel(\phi)$ and $I_\perp(\phi)$ need to be added up. It is then found that the total intensity response function is given by

$$I(\phi) = I_\parallel(\phi) + I_\perp(\phi) = A_{\mathrm{MZ}} - B_{\mathrm{MZ}} \cos(\phi), \tag{2.8}$$

where $A_{\mathrm{MZ}} = 0.188 \cdot I_0$ and $B_{\mathrm{MZ}} = 0.094 \cdot I_0$ are fitting parameters, and I_0 is the initial laser beam intensity.

2.2 Quadrature phase-shift detection

The phase gain of the fraction of the beam that entered the cavity becomes visible in the appearance of the interference pattern, which is described by a sinusoidal function for both interferometers. By either monitoring the movement of the interference fringes or the entire interference pattern, the phase change can be determined. While a fiber is being heated, the fringes in the interference pattern move outward. Vice versa, upon cooling the fiber, the fringes move inward. The movement of the fringes could be monitored by a single detector positioned in the interference pattern. Yet, with the data of one detector measuring changes in light intensity, the direction of the movement of the fringes would be unknown, i.e., heating and cooling of the fiber would be indistinguishable in the data.

A more sophisticated approach is to position two detectors in quadrature inside the interference pattern. This allows not only to detect changes in light intensity but also to identify an increase or decrease in the phase change, i.e., heating and cooling of the fiber are distinguishable. The quadrature phase-shift (QPS) detection, which is discussed in detail in Ref. [33] and **Paper II**, is outlined here in the case of heating an optical fiber with a CO_2 laser for a duration

of 2 s. The HeNe laser is carefully aligned to probe the fiber at the position of the CO_2 laser spot in the FPI configuration. Further, two sensors are positioned $\frac{\pi}{2}$ out-of-phase in the back-scattered interference pattern. A typical plot of the intensity measured by the two sensors is shown in Fig. 2.7(a). The laser is shuttered at 0.2 s, the laser beam heats the optical fiber, which consequently expands, and its refractive index increases [34]. This causes the interference fringes to move outward (compare Fig. 2.3(a) to (d)) across the sensors. This movement can be seen in the intensity signals that start to oscillate once the laser is shuttered. The Lissajous plot of the identical data is shown in Fig. 2.7(b). This plot can be used before an experiment to
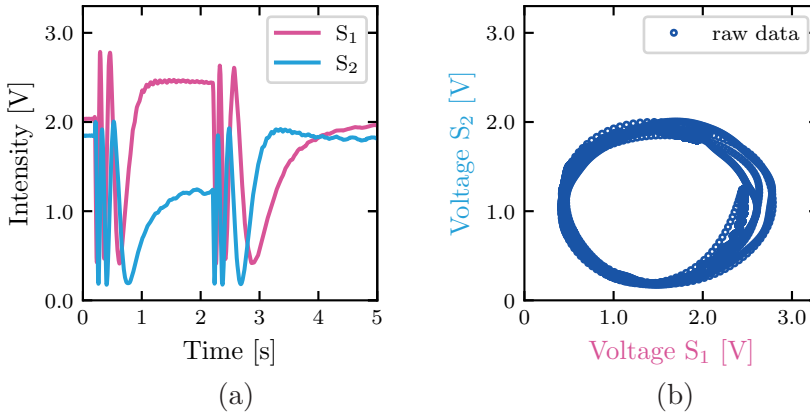
Figure 2.7: (a) Plot of the raw data and (b) Lissajous plot of the raw data obtained from sensors S_1 and S_2.

position the sensors as close to quadrature as possible. In quadrature, the Lissajous plot should be a perfect circle. Moving the sensors out of quadrature will first show an ellipse in the Lissajous plot that converges to a diagonal line for a sensor placement of π out-of-phase. Normally, a perfect circle is hard to achieve due to limited precision in the positioning of the sensors and small production-related variances in the sensitivity of the two sensors. However, small deviations from quadrature do not have a significant impact on the measurement error [33] (see also Section 2.4). The different sensitivities are compensated for during data processing, in which the data is normalized and offset. The processed data is shown

in Fig. 2.8(a). The identical data is shown in Fig. 2.8(b) to emphasize how the phase circulates with time. Data processing can either
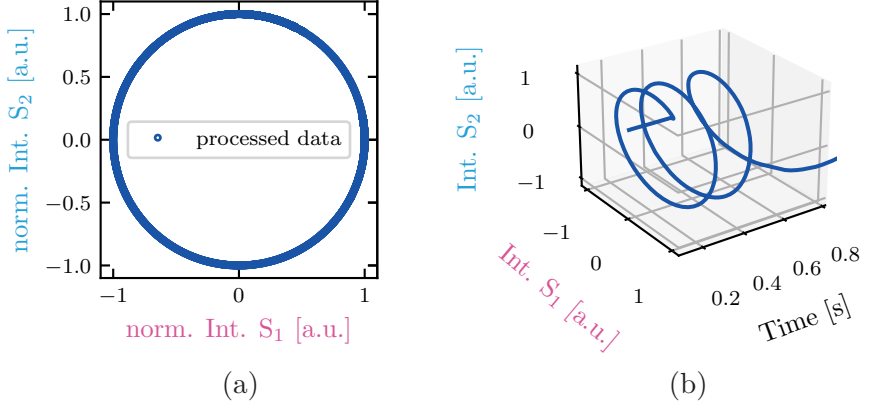

Figure 2.8: (a) Lissajous plot of the processed data. (b) Plot of the processed data as a function of time.

be done after the measurement or in real-time by finding suitable offset parameters apriori. This data processing does not affect the measurement outcome since the latter purely relies on the phase relation between the two sensors. The next step is to apply an arctangent function to the normalized data points to obtain the wrapped phase shown in Fig. 2.9(a). The last step to get the final unwrapped phase change $\Delta\phi$ plotted in Fig. 2.9(b) is to compensate for the phase jumps in the arctangent function.

2.3 Temperature calibration

The last missing step to obtain the temperature of the optical fiber by measuring the unwrapped phase change is a suitable calibration to temperature change. One way of calibration is utilizing an optical fiber with an inscribed regenerated fiber Bragg grating, also known as chemical composition grating (CCG) [35, 36]. The calibration procedure is explained in detail in **Paper I** and consists of two parts.

In the first part, an optical fiber with an inscribed CCG is put adjacent to a K-type thermocouple in an oven (*Carbolite CWF 1100*).
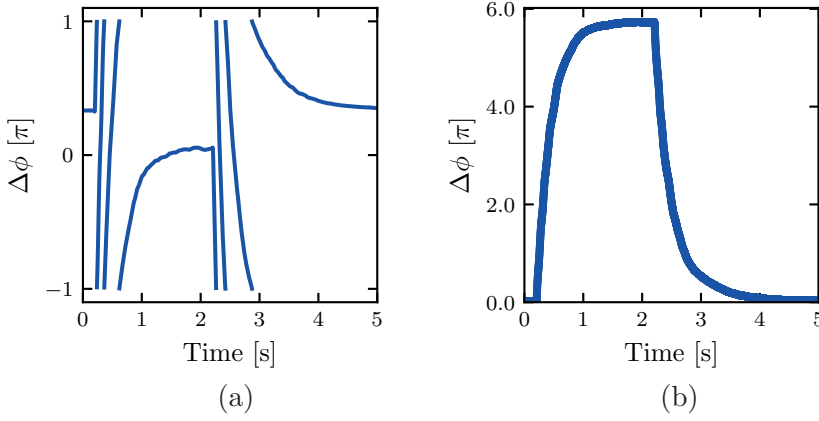
Figure 2.9: (a) Plot of the wrapped phase. (b) Plot of the phase change after phase unwrapping.

The spectrum of the grating is measured in reflection using a supercontinuum white-light source (*Koheras SuperK*) and an optical spectrum analyzer (*Bayspec FBGA-IRS*). The temperature corresponding to the voltage output of the thermocouple is recorded by a data logger (*Picoscope TC-08*). The oven is heated up to $1000\,°C$ in $100\,°C$ increments. At every temperature step, it is made sure that the oven has ample time to stabilize the temperature. The Bragg wavelength shift $\Delta\lambda_B$, and the temperature change ΔT are recorded for every temperature setting. Three typical reflection spectra are shown in Fig. 2.10(a). The obtained data can be used for the calibration shown in Fig. 2.10(b). The dependence of Bragg wavelength shift on temperature change is fitted by the second-order polynomial

$$\Delta\lambda_B = \bar{a} \cdot \Delta T + \bar{b} \cdot \Delta T^2, \tag{2.9}$$

where $\bar{a} = 1.009 \cdot 10^{-2}\,\text{nm}\,°C^{-1}$ and $\bar{b} = 6.711 \cdot 10^{-6}\,\text{nm}\,°C^{-2}$ with a root-mean-square error (RMSE) of $\pm 87\,\text{pm}$ corresponding to $\pm 7.2\,°C$.

In the second part, the relation between Bragg wavelength shift and phase change of the interferometer needs to be calibrated. Therefore, the fiber is heated at the position of the CCG by a CO_2 laser. Simultaneously, the fiber is probed at the same spot by a HeNe laser to measure the phase change in the back-scattered interference pattern as shown in Fig. 2.11. This is shown here for a FPI configuration
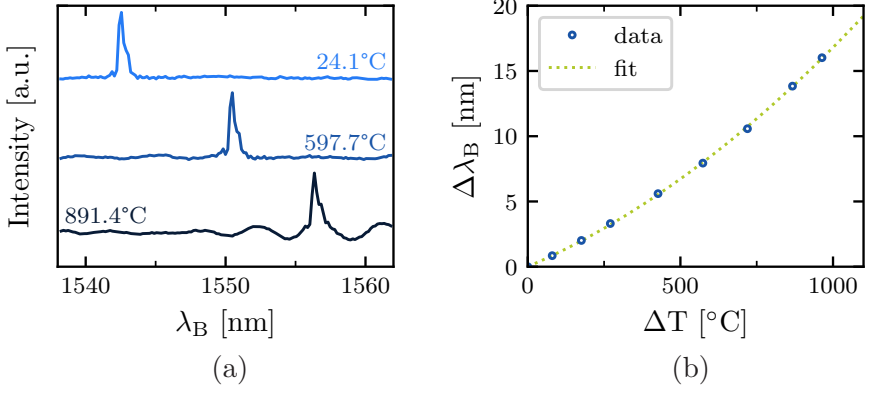
Figure 2.10: (a) Plot of the reflection spectrum of the CCG for three temperatures. (b) Plot of the Bragg wavelength shift of the CCG depending on temperature.

but can analogously be done for a MZI configuration as discussed in **Paper IV**. By measuring both, the Bragg wavelength shift $\Delta\lambda_B$ and the phase change $\Delta\phi$, the two can be related as shown in Fig. 2.12(a). The linear fit is given by

$$\Delta\lambda_B = 0.423 \cdot \Delta\phi. \tag{2.10}$$

A calibration for the dependence of the phase change on temperature is obtained by combining Eq. (2.9), the dependence of the Bragg wavelength shift on temperature, and Eq. (2.10), the relation between Bragg wavelength shift and phase change. The calibration is shown in Fig. 2.12(b) and fitted by

$$\Delta T = a_1 \cdot \left(\sqrt{1 + b_1 \cdot \Delta\phi} - 1 \right), \tag{2.11}$$

where $a_1 = 7.771 \cdot 10^2 \, °C$ and $b_1 = 1.064 \cdot 10^{-1} \, \text{rad}^{-1}$ with a RMSE of $\pm 7.2 \, °C$. As a concluding remark to this section, it should be said that the presented temperature measurement technique is a relative measurement.
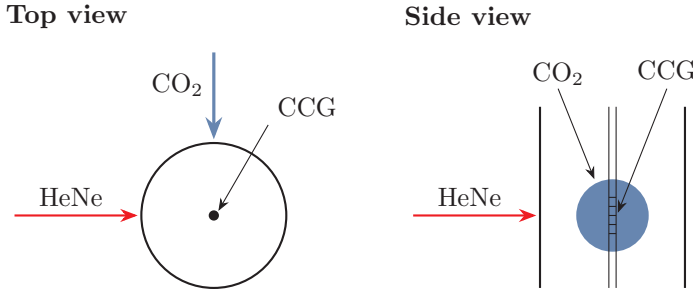
Figure 2.11: Sketch of the alignment to determine the relation between Bragg wavelength shift and phase change of the Fabry-Pérot type interferometer.

2.4 Error analysis

The phase change of the interferometer with temperature is calibrated using a CCG, which is in turn calibrated using a K-type thermocouple. This can lead to an accumulation of error. The various error sources and their influence on the measured temperature are discussed in this section.

One source of error is the temperature calibration of the CCG. To minimize this error, it is crucial to ensure a uniform temperature distribution around the CCG and the thermocouple while calibrating within an oven, and reduce the influence of convection as much as possible. Therefore, each was sleeved by a fused silica tube and put together inside one ceramic tube. This ceramic tube was then placed in the oven. The difference in measured temperature is estimated to be less than $1\,°C$ due to the almost completely enclosed housing around grating and thermocouple, and them being positioned adjacent to each other, only separated by thin ($1\,mm$ wall diameter) fused silica tubes. Further, the accuracy of a K-type thermocouple is specified as the maximum of $\pm2.2\,°C$ and $\pm0.75\,\%$. For the presented calibration (see Section 2.3) this corresponds to a maximum error of $\pm7.5\,°C$ at $1000\,°C$. This means that the found calibration with a RMSE of $\pm7.2\,°C$ is within the uncertainty in the temperature measurement of the thermocouple. The total error of the temperature is then
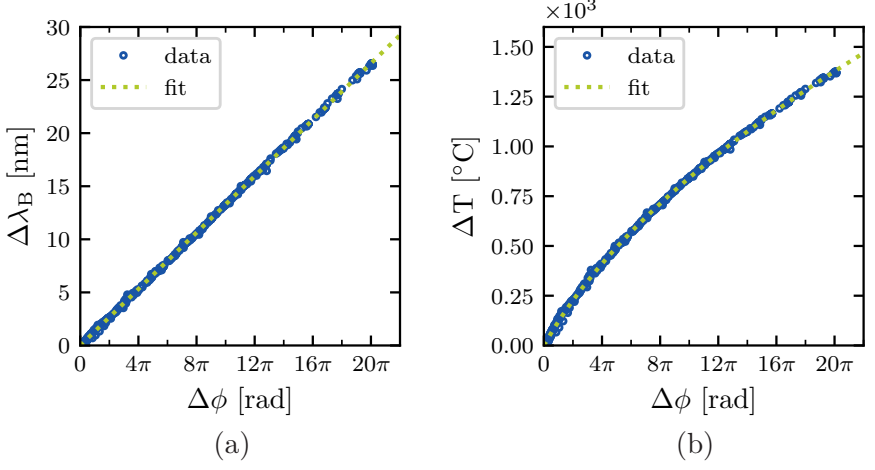
Figure 2.12: (a) Plot of the measured Bragg wavelength shift of the CCG and the corresponding phase change in the interference pattern. (b) Plot of the final temperature calibration for a 125 μm diameter fused silica optical fiber.

smaller than the sum of the positional error inside the oven, and the temperature uncertainty of the thermocouple, i.e. $\leq 8.5\,°C$.

The second source of error is the phase measurement. It can be seen in Fig. 2.7(b) that typically measured data is not perfectly circular but has a slightly elliptical shape to it. The reasons are, as discussed in Section 2.2, different sensitivities of the two sensors and their positioning in the interference pattern slightly off quadrature position. The effect on the measured phase change and an in-depth error analysis has been conducted in Ref. [33]. It was found that displacement of the sensors in the interference pattern up to $10°$ off the ideal out-of-phase position do not "substantially increase the decoding error." The same was true for up to $40\,\%$ amplitude modulations, i.e., differences in sensor sensitivity. Typically, the resulting decoding error was found to be less than $6.25 \cdot 10^{-3}\,\%$. Additionally, in **Paper IV** a calibration for the temperature change on phase change for the MZI configuration was derived and is given by

$$\Delta T = a_2 \cdot \left(\sqrt{1 + b_2 \cdot \Delta\phi} - 1 \right), \tag{2.12}$$

where $a_2 = 6.502 \cdot 10^2\,°C$ and $b_2 = 1.081 \cdot 10^{-1}\,rad^{-1}$ with a RMSE of $\pm 3.0\,°C$. Using Eq. (2.12), a relative error of $\pm 6.25 \cdot 10^{-3}\,\%$ in the phase measurement corresponds to a temperature error of $\pm 4\,°C$ at $1000\,°C$.

Another source of error can be a lack of knowledge of the exact shape of the optical fiber. If it is elliptical, the actual OPL is different from the ideal case shown in Fig. 2.4(b) and Fig. 2.4(c). An ellipticity of only 0.99 causes deviations in the measured temperature from the actual temperature by $19.0\,°C$ at $1000\,°C$ as has been demonstrated in Ref. [37].

Last, the temperature calibration for a MZI demonstrated in **Paper IV** was done on a fused silica fiber with a germanium doped core. This means that the core and cladding of the fiber had similar thermal expansion coefficients and did not cause pressure-induced refractive index changes. For a different core material such as silicon that has a thermal expansion coefficient of approximately a factor four [38] larger than the silica cladding, pressure-induced refractive index changes are a possible source of error. Additionally, silicon has a volume increase of $9\,\%$ upon freezing [39] which could affect high-temperature measurements drastically. Thus, in the case of SCFs, it is necessary to consider the refractive index to be dependent on temperature and pressure. The following thought experiment to estimate the inbuilt stress can indicate the resulting error. During fabrication of the SCF, the silicon core is still molten when the outer fiber has already cooled and set at its final diameter value of $125\,\mu m$. When the silicon solidifies, it expands and puts the cladding under pressure. For a $20\,\mu m$ silicon core, the density of the silica cladding is increased by 1.002. It can be calculated that the refractive index is increased from $n_0 = 1.4570$ to $n = 1.4578$, following the relation between the refractive index of silica glass and its density given in Ref. [40]. The resultant phase error is $0.55\,\%$, which corresponds to a temperature error of $\pm 4.1\,°C$ at $1000\,°C$ [37].

Adding up all the different error sources, the temperature measurement is precise to within $\Delta T = \pm 35.6\,°C$ at $1000\,°C$. The main source of error here is the assumption of a slightly elliptical fiber. By determining the exact dimensions of the fiber, the measurement error can easily be reduced by $19\,°C$. The second-largest error source

is the calibration with the K-type thermocouple. The error in the measurement of the phase and the error caused by the refractive index change in SCFs minimally contribute to the accumulated measurement error.

3 Laser processing system

The fiber processing presented in this thesis was based on a laser processing system that consisted of the following parts: a carbon dioxide (CO_2) laser, a laser control system, and a fiber processing setup, as illustrated in Fig. 3.1. The first section of this chapter
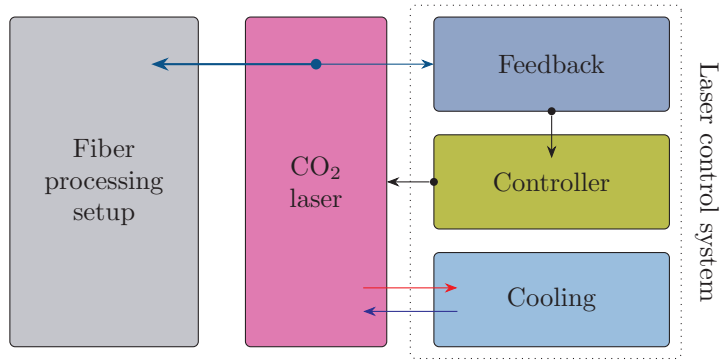

Figure 3.1: Block diagram of the laser processing system.

starts with a short introduction to the working principle of CO_2 lasers. Then, the three components of the laser control system are discussed. One component is the feedback setup that together with the second component, a specialized controller, stabilized the laser output regarding absorption in fused silica glass. The third component is the cooling system that contributed to the laser stabilization as well. The controller was extended into a fully automated control system for the fiber processing setup, which is described in detail in the last section of this chapter.

3.1 Carbon dioxide laser

A preliminary report on laser action in CO_2 [41] came just before the formal introduction of the CO_2 laser in 1964 by C. Patel [42]. The working principle of this gas laser, usually comprising a mixture of CO_2, N_2 and He, is described in Ref. [43, 44]. It relies on rotational-vibrational transitions of the CO_2 molecule. The three non-degenerate vibrational modes of the triatomic molecule are a symmetric stretching mode (ν_1), a bending mode (ν_2) and an asymmetric stretching mode (ν_3) as illustrated in Fig. 3.2. The energy levels of the three modes are
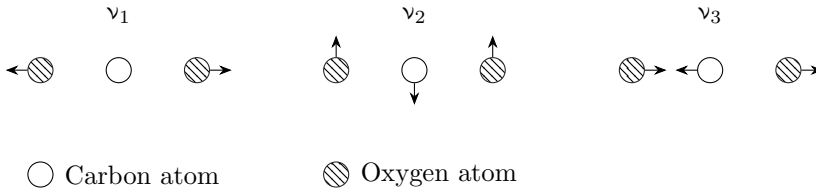
Figure 3.2: Sketch of the three fundamental vibrational modes of the CO_2 molecule.

sketched in Fig. 3.3. The CO_2 molecule is efficiently excited into the asymmetric stretching mode ν_3 due to two mechanisms. One mechanism is collisions with electrons, and the other one is energy transfer from nitrogen molecules that have a comparable excited energy state as ν_3. The lasing transitions are between the asymmetric stretching mode and both the bending and symmetric stretching mode. The transitions have an energy difference that corresponds to a wavelength of $\lambda = 9.4\,\mu m$ and $\lambda = 10.4\,\mu m$, respectively. The rotational levels are populated according to the Boltzmann distribution, which causes the predominant rotational-vibrational transitions to actually emit wavelengths of $\lambda = 9.6\,\mu m$ and $\lambda = 10.6\,\mu m$. Lasing also occurs on many other rotational lines [42]. Those lines are in practice filtered by a Littrow grating [44]. The remaining broadening of the output laser line can be attributed to the Doppler effect and collision broadening. For continuous laser operation, the lower vibrational modes (ν_1, ν_2) have to be depleted. This is done through inelastic collision with helium atoms.
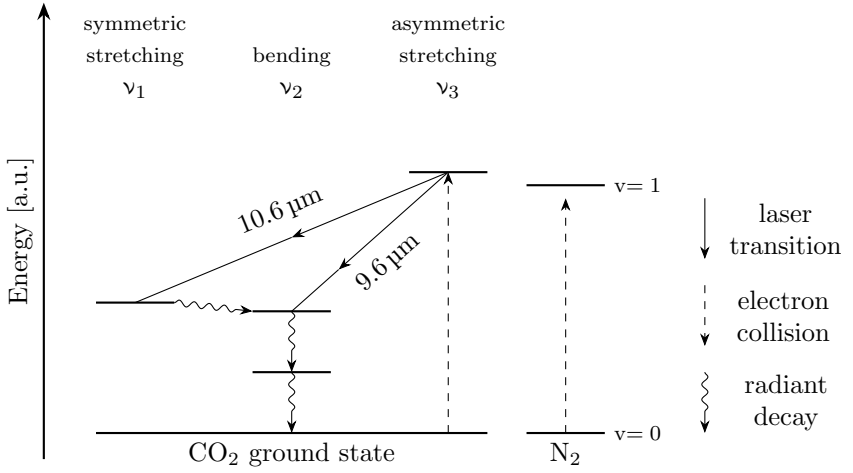
Figure 3.3: Energy diagram of the ground electronic state of a CO_2 molecule. For clarity, only the lowest vibrational and no rotational levels are shown.

3.2 Laser control system

The CO_2 laser used in this thesis was a *Synrad Firestar ti100HS* with an output power up to 100 W and a heat load of 1.7 kW. It had a power stability of $\pm 2\,\%$, insufficient for some fiber processing applications. The main contributions to the unstable power output of a CO_2 laser are changes in laser line and variations in cavity length mainly induced through temperature fluctuations. While the laser line for this particular laser was according to the specifications stabilized at $\lambda = 10.60 \pm 0.03\,\mu\text{m}$, there was no possibility to stabilize the cavity length. In this thesis work, the laser output was stabilized regarding induced heat in silica by two methods. One, was the developed cooling system that targeted stabilization of the laser output power by keeping the temperature of the laser as constant as possible. The other one was active stabilization of the laser with a specialized controller monitoring the output fluctuations of the laser in a feedback setup.

3.2.1 Cooling system

A schematic of the cooling system used to cool the CO_2 laser is shown in Fig. 3.4(a). Initially, the heat load of the laser was only removed by an industrial water cooler (*Deltatherm LTK 1.4*). It had a cooling power of $1.8\,\mathrm{kW}$ and provided cooling water with a temperature range of $\approx 1\,\mathrm{K}$ around the set temperature. While the large cooling power was needed to operate the laser at high powers, it was over-dimensioned for the typical lab applications at up to $70\,\%$ of the maximum output power. As can be seen in Fig. 3.4(b), the unstable cooling water temperature T_w of the industrial chiller caused an unstable temperature of the laser and ultimately an unstable laser power P_l. Therefore, three components were added to the cooling

(a)   (b)
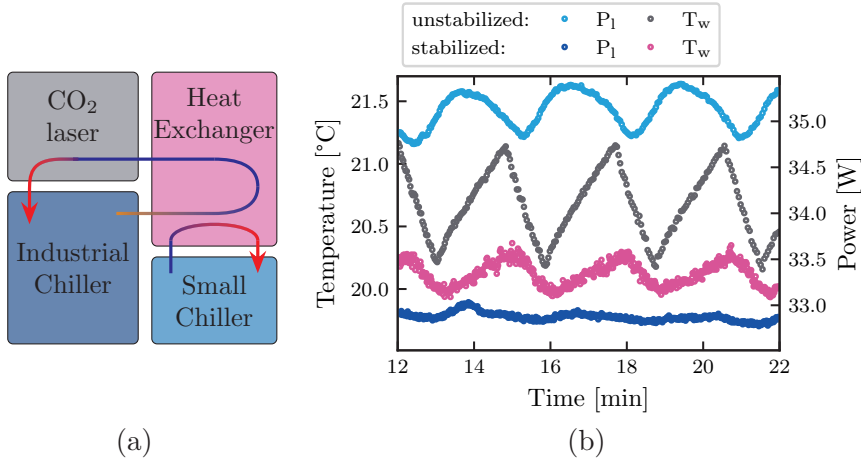
Figure 3.4: (a) Block diagram of the cooling system implemented to stabilize the cooling water temperature. (b) Plot of the measured temperatures of the cooling water T_w and the output power P_l of the CO_2 laser before and after stabilization.

system to stabilize the temperature of the cooling water and thereby the laser output power. One was a flowmeter inserted into the cooling line that regulated the water flow down to $3.8\,\mathrm{L/min}$. Additionally, a second chiller (*SMC HECR006-A5*) with a cooling power of $600\,\mathrm{W}$ and a temperature stability of $\leq 0.1\,\mathrm{K}$ was used to stabilize the precooled water of the industrial chiller via the third component, a

heat exchanger. The final cooling system was able to stabilize the cooling water temperature ($\Delta T = 0.4\,\mathrm{K}$) and thereby the laser power to within $\pm 0.5\,\%$ as shown in Fig. 3.4(b).
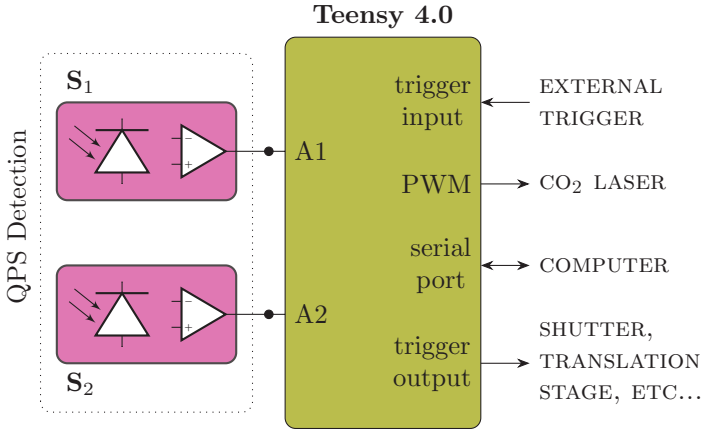
3.2.2 Controller

The CO_2 laser was controlled by providing a pulse-width-modulated (PWM) radio-frequency signal to the input electronics of the laser. The laser power was set by adjusting the length of the on-pulse of the PWM signal. In the beginning, the laser was driven by a commercial controller. One percent of the CO_2 laser beam was tapped by an anti-reflection (AR) coated ZnSe plate beamsplitter and monitored with a power meter (*Thorlabs S314C*). This setup had several disadvantages. One was that the laser controller allowed only for adjustment of the laser power in steps of $1\,\%$ dutycycle. The laser operated at full output power at $50\,\%$ dutycycle, which meant that the smallest possible stepsize corresponded to more than $2\,\mathrm{W}$ of output power, too much for precise processing of SCFs. Another disadvantage was that the *Thorlabs S314C*, as is typical for power meters, had a response time of $\approx 1\,\mathrm{s}$, too slow for fast active feedback to the laser. Furthermore, as the name *power meter* suggests, the measured variable is power. However, for the processing of silica clad fibers, it is more important to know to which temperature the fibers are heated by the CO_2 laser beam coupled through the absorption coefficient. The absorption coefficient of fused silica is not constant around $10.6\,\mathrm{\mu m}$ [6] making it sensitive to the active laser line. So an ideal system for laser stabilization should

- allow for fine control over the PWM signal,

- monitor power variations concerning induced heat in silica,

- and give direct feedback to the PWM signal.

The main component of the new controller was a *PJRC Teensy 4.0* microcontroller as illustrated in Fig. 3.5. It controlled the output power of the laser by setting an appropriate PWM signal with a 12-bit resolution. During development, even smaller steps in the PWM signal were tested. However, no change in laser output power was observed

Figure 3.5: Sketch of the developed laser controller.

for changes in the PWM signal smaller than $0.01\,\%$. Furthermore, the controller measured the laser output via QPS detection (see Chapter 2) for active stabilization as described in Section 3.2.3. Additionally to the controlling and monitoring function of the laser power, several trigger in- and outputs were added to the microcontroller. This allowed for synchronization of all measurement equipment such as shutter and translation stages, but also optical spectrum analyzers as sketched in Fig. 3.5.

3.2.3 Feedback setup

A second function of the microcontroller was monitoring of the induced heat in fused silica by the CO_2 laser. The measurement setup to obtain the induced temperature is shown in Fig. 3.6 and is an application of **Paper I** [45]. The beam of the CO_2 laser was linearly polarized and split into two by an AR-coated ZnSe wedge. The main part of the beam transmitted into the fiber processing setup. Approximately $10\,\%$ of the beam was outcoupled by the wedge and reflected onto a $200\,\mu m$ fused silica fiber which acted as a feedback sensor. It was probed by the focused beam of a HeNe laser. A quarter wave-plate ($\lambda/4$) and a polarizing beam splitter (PBS) ensured that only reflections from the fiber were incident on the sensors S_1 and S_2. The temperature of
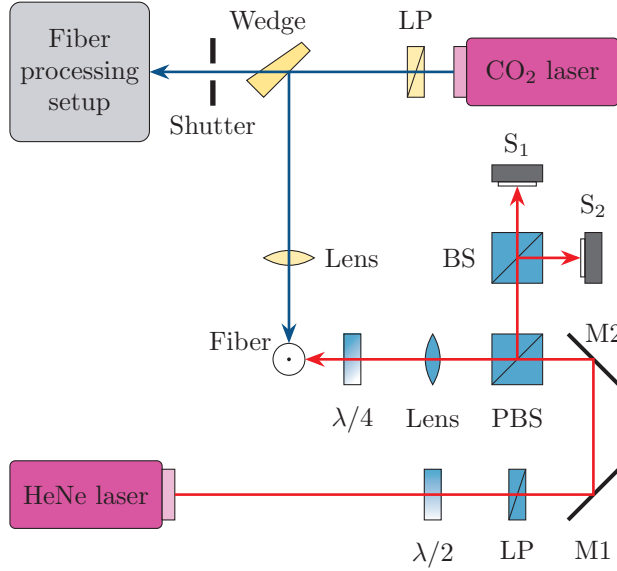
Figure 3.6: Sketch of the feedback setup.

the fiber was measured by QPS detection as explained in Chapter 2. The analog voltage given by the two sensors placed in the interference pattern was read by the microcontroller and sent to a computer via a serial connection for data processing. The induced temperature, derived from the measured phase, served as a reference for laser monitoring and stabilization. Furthermore, the response time of the fused silica fiber was investigated and found to be ≈ 300 ms. Here, the response time was defined as the time the fiber needed to cool down to $1/e$ of the initial temperature upon closing the shutter of the CO_2 laser.

The stabilization was done through a PID loop. After an initial calibration to find a linear relationship between the measured phase and the set PWM signal, the PID loop was optimized to stabilize the measured phase for a given PWM signal. Figure 3.7 shows the measured phase converted to temperature for the stabilized and the unstabilized CO_2 laser at two different laser powers. It can be seen that the laser output was more constant when stabilized via the PID loop. It was possible to reduce the maximum temperature deviation
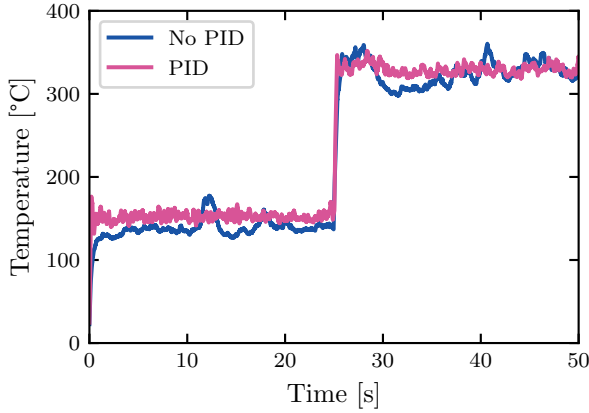
Figure 3.7: Comparison of the induced temperature in the feedback fiber for two different powers with and without stabilization.

from its mean of more than $50\,°C$ down to approximately $25\,°C$ and to halve the standard deviation as well. However, the presented stabilization was optimized regarding a $200\,\mu m$ fused silica fiber. A smaller fiber would be more sensitive and responsive at the cost of not being as durable. Further, the stabilization focused on reducing long-term drifts in the order of seconds to minutes. In Fig. 3.7 it can also be seen that the short-term stability of the unstabilized laser was often better than in the stabilized case.

A crucial component in the feedback setup shown in Fig. 3.6 was the beamsplitter, an AR-coated ZnSe wedge that outcoupled $10\,\%$ of the laser power for monitoring. Several experiments have been conducted to find a suitable beamsplitter for the feedback setup. All AR-coated plate beamsplitters were found to be unsuitable and did not produce reliable results. Most likely, this is explained considering two reflections of the beamsplitter initiating from the back and front side despite the AR-coating. The heat induced by the incident laser beam changed the thickness of the beamsplitter. Consequently, the two reflected beams interfered differently. Since the sensor was now a fiber and not a detector with a big aperture, the changed local intensity altered the measured phase, although the overall intensity of the laser did not change.
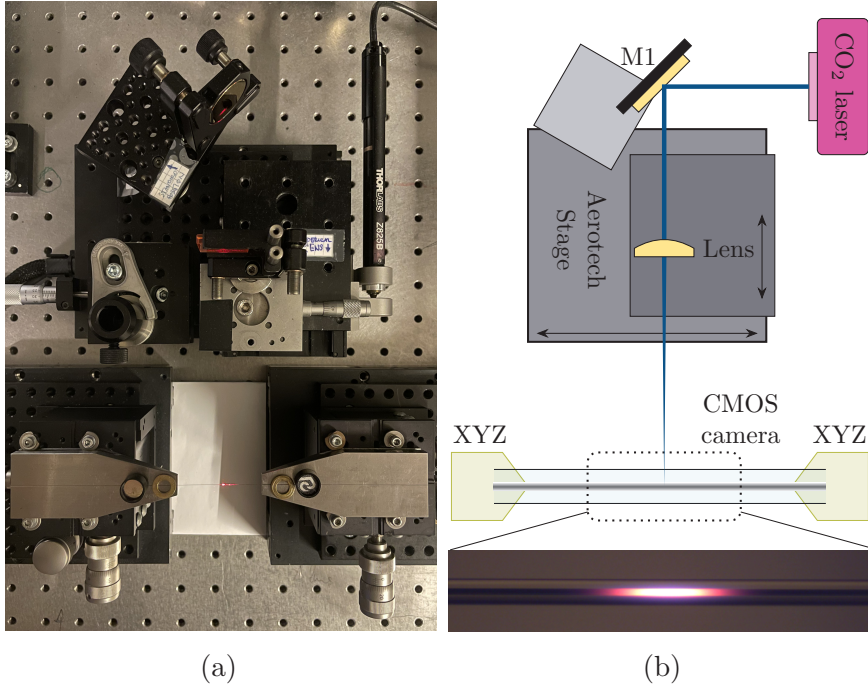
3.3 Fiber processing setup

The fiber processing setup is shown in Fig. 3.8. For processing, the fibers were horizontally suspended in air and magnetically clamped into XYZ-grooves, which were fixed on XYZ-stages. The beam of the CO_2 laser beam was tapped by a wedge and stabilized with the help of the feedback setup, as explained in Section 3.2.3. The main part of the beam was reflected by a golden mirror mounted on top of a translation stage (*Aerotech ALS130H-50*) onto the SCFs that were being processed. The laser beam could be scanned along the fiber by moving the translation stage. To ensure uniform heating across the whole fiber diameter, the laser beam was focused horizontally by a cylindrical lens ($f = 127\,\mathrm{mm}$) to form a vertical line. This lens was mounted on top of a second translation stage that could be moved perpendicular to the *Aerotech* translation stage to adjust the position of the focus point with respect to the fiber. Additionally, a CMOS camera (*Thorlabs DCC3240C*) was mounted on top of the translation stage. This camera was aligned to capture the heat zone of the fiber and could monitor the fiber core through the transparent cladding.

3.3.1 Characterization of the laser beam

The shape of the beam significantly impacts the heating dynamics in the SCF and was carefully investigated. The shape of laser beams can typically be determined by scanning a structured mechanical part such as a knife-edge, a pinhole, or a slit through the beam and simultaneously measuring the transmitted power with a detector. An initial attempt to utilize such a method to determine the beam shape was made without success. Even at the lowest power at which the CO_2 laser could operate ($P = 3.7\,\mathrm{W}$), the mechanical parts used, such as a razor blade or a fused silica plate, either deformed, were destroyed or started radiating themselves. So an alternative approach had to be found.

The solution was to scan the laser beam across a fiber with an inscribed CCG (similar to the grating used for temperature calibration in Section 2.3). The fiber was mounted vertically as illustrated in Fig. 3.9. The setup used to scan the laser beam across the fiber is otherwise identical to the fiber processing setup shown in Fig. 3.8.

(a)   (b)

**Figure 3.8:** (a) Photograph and (b) sketch of the fiber processing system.

The optical fiber was connected to a white-light source (*Koheras SuperK*) and the CO_2 laser beam was scanned across the fiber at the position of the CCG. The resulting shift of the Bragg wavelength was monitored with an optical spectrum analyzer (*Bayspec FBGA-IRS*). Since the Bragg wavelength shift corresponded to the heat absorbed by the fiber and thus the CO_2 beam intensity, the beam shape could be determined.

As the fiber, mounted on top and hanging freely, would uncontrollably move if scanned through the laser beam, the fiber was fixed in one position, and the beam was scanned over the fiber by moving the translation stage instead. To obtain a full beam profile around the focal point of the lens, the beam was scanned across the fiber at multiple positions around the beam waist. Since the fiber had a finite width, the measured back-reflection corresponded to a convolution of
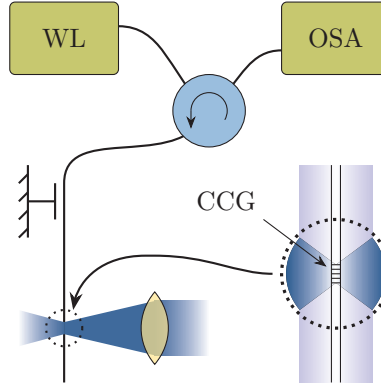
Figure 3.9: Sketch of the vertically mounted fiber containing a fiber Bragg grating.

a rectangular function with a Gaussian function. Typical data for the measured normalized Bragg wavelength shift for one scan is shown in Fig. 3.10(a). This scan was executed at ten positions around the focus and the obtained beam widths are plotted in Fig. 3.10(b) fitted by $w(z) = w_0\sqrt{1 + (z/z_R)^2}$, with a Rayleigh range $z_R = 3.693\,\mathrm{mm}$ and a beam waist $w_0 = 122\,\mu\mathrm{m}$. Figure 3.10(c) is a contour plot of the temperature within the laser beam around the focus. The plot shows an interpolation between the measured data points. The Bragg wavelength shift was converted to temperature using Eq. (2.9).
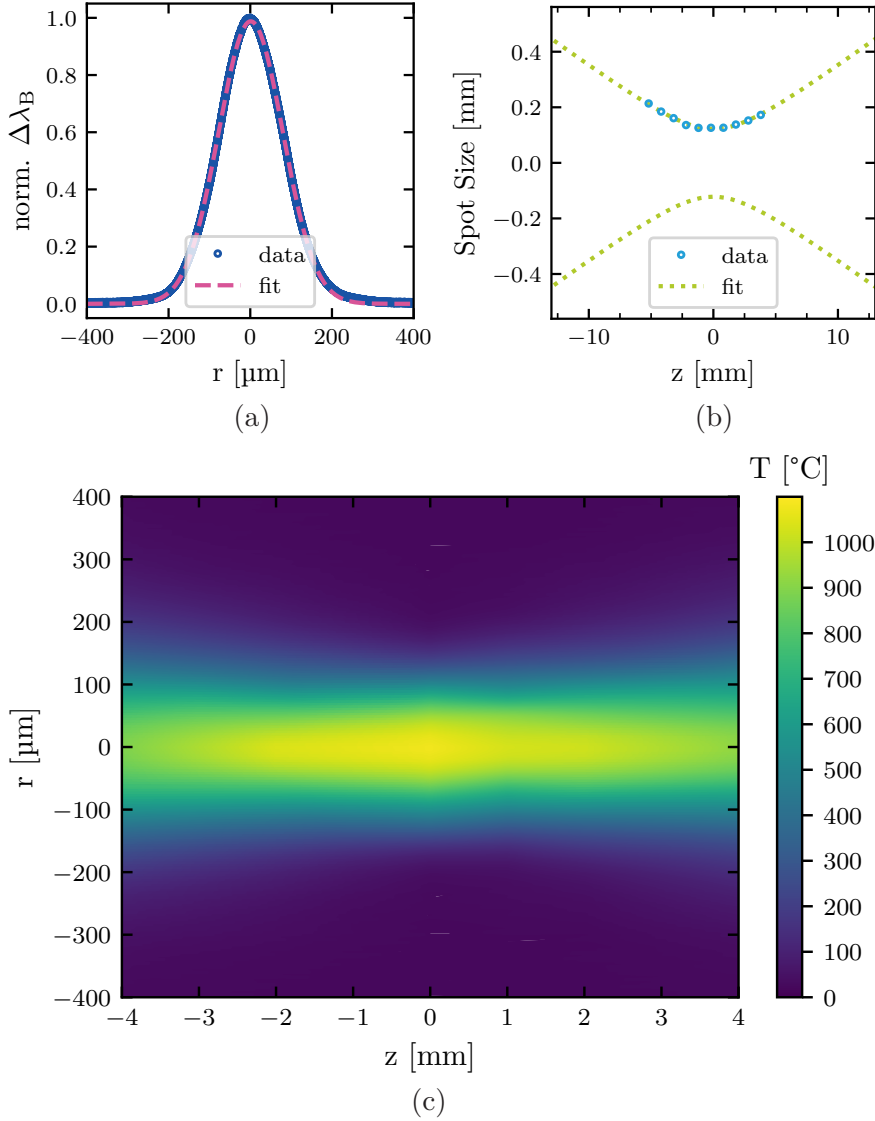
Figure 3.10: (a) Plot of the normalized Bragg wavelength shift for a transversal line scan through the CO_2 laser beam. The fit is the convolution of a rectangular function and a Gaussian function. (b) Axially measured beam widths. (c) Contour plot of the beam intensity as a function of induced temperature in the CCG.

4 Fiber manufacturing

Optical fibers in general and silicon core fibers in particular are often fabricated by heating and softening a so-called preform, a scaled-up duplicate of the desired fiber. The softened preform is then drawn into the final thin fiber. The following section starts with a brief overview of preform manufacturing before it focuses on the developed experimental laser-based fiber draw tower.

4.1 Preform system

Preforms are typically manufactured by techniques such as modified chemical vapor deposition (MCVD). The desired chemicals, typically silicon dioxide or germanium dioxide, are precipitated from precursors, usually the corresponding tetrachlorides, onto the inside of a silica tube. The core material is fused layer-by-layer by a traveling burner that heats the gases to around 1800 K [46]. The final preform is obtained in the last step by collapsing the tube after deposition is completed. MCVD, while leading to outstanding silica-based fibers, is limited in viable glass compositions [47] and is heavily focused on the deposition of oxides [46].

SCF preforms can be made by stacking the desired semiconductor into a silica tube, then fusing core and cladding either by a hydrogen burner or in an induction furnace and sealing the tube at the bottom. However, this exposes the preform to temperatures above 1400 °C for a long time, typically in the order of tens of minutes. This is disadvantageous for the fiber quality since it is likely to contaminate the SCF core by oxygen diffusion from the cladding [21, 23]. Ideally, the time during which the preform is exposed to such high temperatures should be limited as much as possible. This can be done by collapsing the tube onto the core material using the very localized heat zone of a carbon monoxide (CO) laser [48] instead of the hydrogen burner. Laser-based heating has been previously used in fiber fabrication [49,

50], typically focused around CO_2 lasers. The advantage of using a CO laser is its larger penetration depth in silica since it operates at around $\lambda = 5.5\,\mu m$ [6, 51]. Scanning the CO laser beam along the preform, which is rotated around its axis, minimizes processing time and thus diffusion time. The preforms manufactured in such a system were pulled into various fibers using an experimental draw tower, which is presented in Section 4.2.

4.2 Fiber draw tower

In commercial fiber draw towers, heating of the preform is usually done through induction furnaces. Drawing techniques have been brought to perfection to produce vast amounts of all silica fiber at draw speeds in the order of kilometers per minute. Those draw towers span over several stories in buildings specially built for them.

A specialized research tower, in which specialty fibers of different dimensions can be drawn on-demand without wasting vast quantities of energy, is a promising tool to investigate SCFs. Such a tower was built with a laser-based furnace at its core (see the appended **Paper III**). The tower and the design of the furnace are shown in Fig. 4.1. On the top, the preform is mounted and held in place by two clamps. One is responsible for positioning, the other one for angular steering of the preform. The preform is then fed into the furnace, which is designed as illustrated in Fig. 4.1(c). The beam of a CO laser is reflected by a mirror that is mounted on top of a voice coil before it is split into four parts equal in power by a grating. Four mirrors (M1-M4) reflect the separated beams onto the preform. Those four beams, together with the oscillating voice coil, ensure uniform heating of the preform. Subsequently, the fiber passes a diameter gauge, and a UV-curable coating is applied. The coated fiber is then threaded through a tensions sensor before it is picked up and wound by a capstan.

The laser-based furnace has several advantages for the manufacture of SCFs. First, the localized heatzone ($\sim$ cm) and the previously mentioned large penetration depth in silica drastically reduce processing time. This limits the possibility for diffusion and dissociation of the cladding into the core and oxidization of the latter [19]. Additionally, the heat zone can be monitored by cameras due to the open furnace
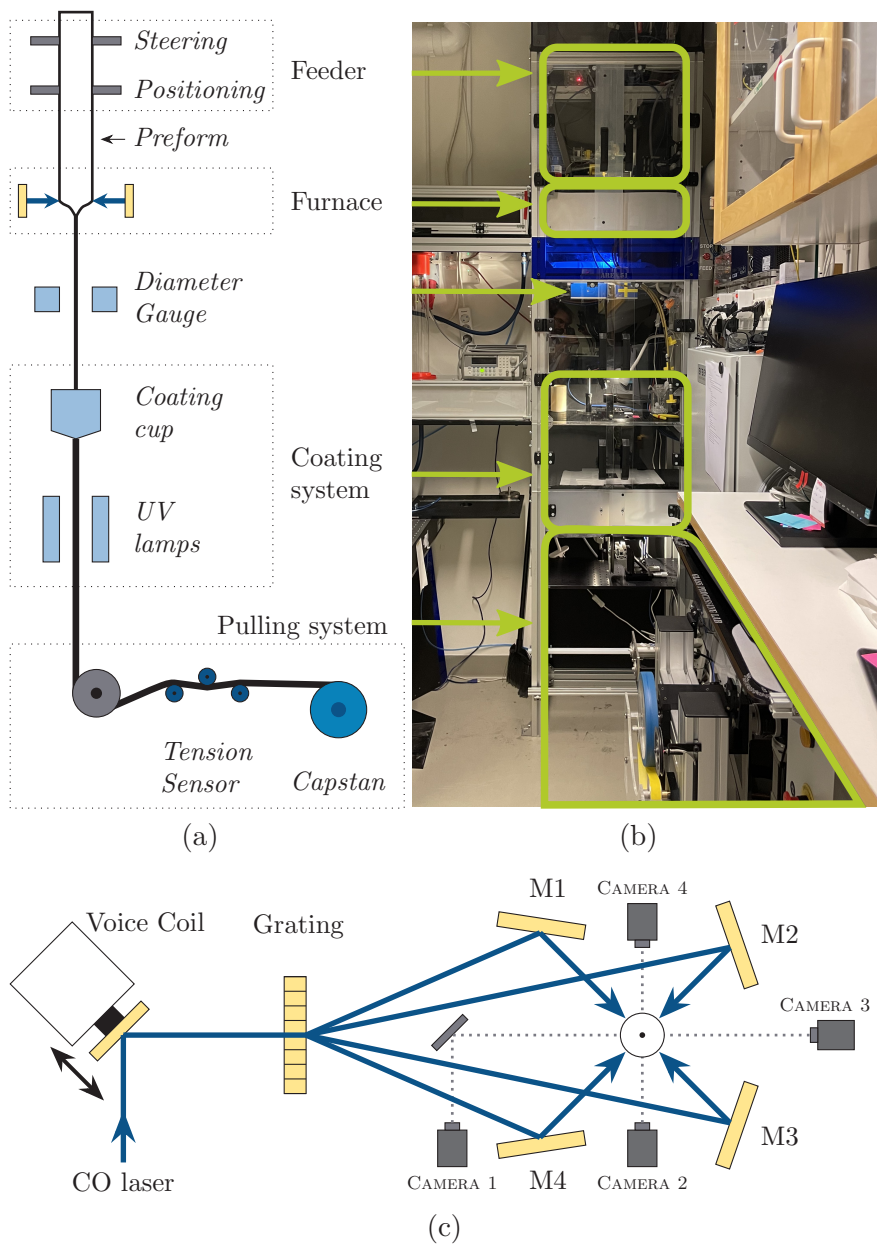
Figure 4.1: (a) Sketch of and (b) photograph of the fiber draw tower. (c) Illustration of the furnace design.

design. Moreover, using a laser as the heat source allows for the compact footprint regarding its size as well as power and cooling demand. This draw tower is only 2.8 m tall and can conveniently be operated by a single person. This is possible since all components of the draw tower are computer-controlled by a self-written *python* program.

The fully computer-controlled draw tower opens the window for additional functionality. The measured diameter at the diameter gauge is compared with a previously set desired fiber diameter, and the draw speed at the capstan adjusts accordingly to keep a constant fiber diameter. Another feedback is given by the tension sensor to the CO laser. Again, a desired range for the draw tension is set apriori. If the measured tension is outside this range, the laser power is adjusted. Those feedback systems help to keep draw parameters as constant and comparable as possible and are also an almost indispensable feature for drawing SCFs. There is a transition in the preform when going from the sealed silica bottom into the region with a silicon core. At this point, the higher thermal conductivity of silicon compared to silica [52, 53] suddenly requires a higher laser power to keep the glass soft. Furthermore, a very controlled drop-off is feasible since the heat source can be taken away almost instantaneously by shuttering the laser. Moreover, a fiber draw can be interrupted in the middle and continued on another day.

The draw tower presented here was used to fabricate various types of fiber, e.g., all-glass titanium dioxide doped fibers, but was mainly optimized and used to produce SCF. Fibers were typically drawn at $10 \, \mathrm{m \, min^{-1}}$, but faster draw speeds were tested successfully as well. The draw speed was mainly limited by the preform size. On the one hand, the preform length was restricted by the size of the upper draw tower section labeled *Feeder* in Fig. 4.1. Hence, after a successful drop-off and the fiber being spooled, there was limited time for ramping the draw speed before the end of the preform was reached. On the other hand, the heating power of 300 W of the CO laser limited the diameter of the preform to less than 10 mm. Nevertheless, SCFs drawn at $10 \, \mathrm{m \, min^{-1}}$ already showed optical transmission losses of down to $0.2 \, \mathrm{dB \, cm^{-1}}$ [20].

5 Temperature measurements

In this final chapter, it is outlined how the techniques presented so far allow for in-situ temperature measurements on SCFs during CO_2 laser processing. Additionally, the findings of those measurements are presented.

## 5.1 Laser processing of silicon core optical fibers

Irradiating a SCF with a CO_2 laser beam is a suitable postprocessing technique to alter the properties of the fiber [19]. The laser power is absorbed by the silica-cladding, which can be considered to be opaque at the CO_2 laser's operating wavelength of $\lambda = 10.6\,\mu m$. At room temperature, the penetration depth in silica is $34\,\mu m$ and reduces down to $4\,\mu m$ at $1800\,°C$ [51]. This implies that heating of the silicon core happens through heat conduction from the cladding when the latter is exposed to CO_2 laser radiation.

In the visible spectral range, fused silica is transparent even at high temperatures. This convenient fact enabled visual inspection of the silicon core during processing. This was done by a CMOS camera and a 10x microscope lens mounted on top of the translation stage vertically above the heat zone in the fiber as shown in Fig. 3.8. A typically obtained micrograph of an unheated fiber is shown in Fig. 5.1(a). Figures 5.1(b) - (d) show the same silicon core when exposed to the CO_2 laser beam going from a lower laser power (see Fig. 5.1(b)) to a higher laser power (see Fig. 5.1(d)). It can be seen how the emissive power of the silicon core increased with increasing temperature [54], induced by increasing laser power. In Fig. 5.1(d), the camera exposure time was lowered to prevent oversaturation. It also becomes apparent that the emissivity of silica was significantly lower than the emissivity of silicon. Only the core of the fiber was still visible, while the cladding was not, under the given camera settings. When the laser power was
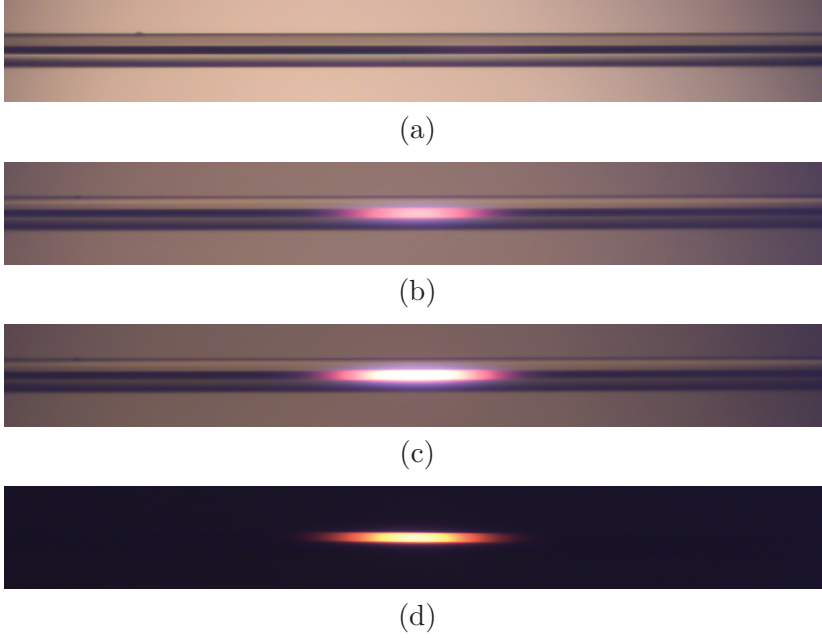
Figure 5.1: Micrographs of a 125 µm diameter silica-clad fiber with a 20 µm silicon core (a) unheated and (b) to (d) heated by a CO_2 laser with increasing laser power.

increased even more, the fiber was heated further until the silicon core melted in the center of the beam. This melt zone can be seen in the micrograph in Fig. 5.2(a). Solid and molten silicon can be clearly distinguished due to a discrete step in emissivity when silicon goes from the solid to the liquid phase. The emissivity of solid silicon in the visible is almost constant $\epsilon = 0.65$ at higher temperatures (540 K to 790 K) [54] and close to $\epsilon = 0.6$ just before melting [55]. The emissivity of liquid silicon is $\epsilon = 0.27$ [55], which made it easy to distinguish the two phases in silicon. Figure 5.2(b) shows intensity profiles of a line scan along the SCF fiber when heated below and above the melting point of the silicon core. There were two distinct peaks visible at the position of the solid-liquid interface for a molten silicon core due to the different emissivities.

(a)

(b)
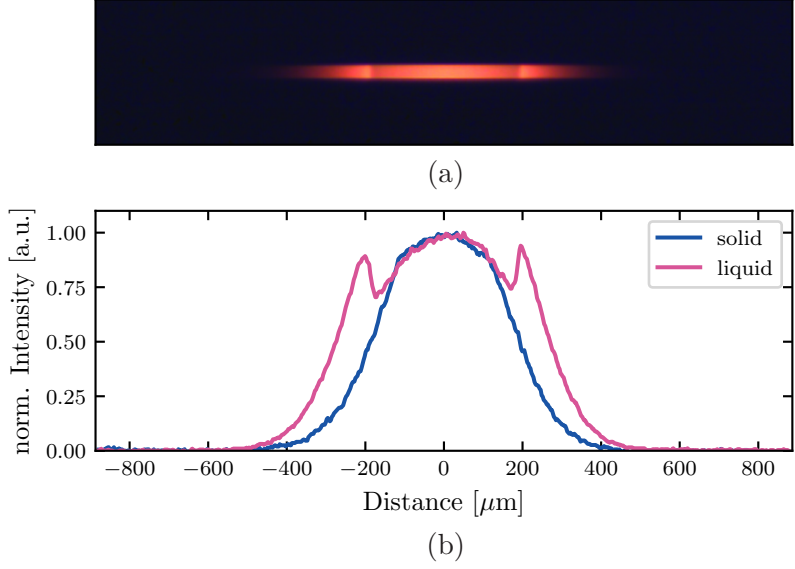
Figure 5.2: (a) Micrograph of a $125\,\mu m$ diameter $20\,\mu m$ silicon core fiber when heated by a CO_2 laser at a high enough power to melt the silicon core (central region). (b) Intensity profiles along the fiber for a solid and a liquid core.

Most CO_2 laser postprocessing techniques rely on moving this melt zone through the fiber in a controlled manner by scanning the laser beam along the fiber. While novel in the fiber geometry, the technique is known as zone melting [5]. Just as for zone melting, it has been shown that it can be used for purification [56], changes in composition [4, 57] and single crystal growth at speeds exceeding millimeters per seconds [26]. As previously mentioned, remelting the core can reduce the losses of a SCF. It was found that by increasing the rate at which the silicon core recrystallizes, the optical transmission losses decrease [26]. Yet, the cooling rate has so far only been estimated from black-body radiation and has not been directly measured. This gap is closed by the presented thesis. The performed in-situ temperature measurements across the melting point of SCFs during CO_2 laser processing are presented in the next section.

5.2 Temperature measurements across the melting point of silicon core fibers

The experimental setup to perform the in-situ temperature measurements was identical to the setup shown in Fig. 3.8 but had an additional temperature measurement system, which is shown in Fig. 5.3. The horizontally suspended fibers were probed at an incident angle
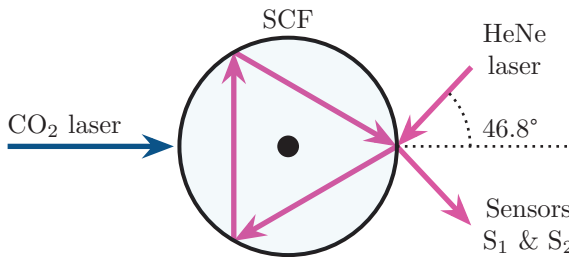
Figure 5.3: Sketch of the temperature measurement system. This interferometer was used to measure the average temperature on a triangular path through the fiber cladding.

of approximately $46.8°$ by a HeNe laser using the cross-section of the fiber as a MZI. Two different types of processing were performed and investigated: stationary processing in which the SCF was heated at a fixed position by the CO_2 laser beam and probed at the same location by the HeNe laser beam; and scanning processing in which the SCF was scanned by the CO_2 laser beam over $2\,cm$ across the fixed temperature measurement point. Both types of experiments, illustrated in Fig. 5.4, were performed at different laser powers and, for the scanning case, also at different velocities. Several factors complicated the realization of this experiment. One was physical restrictions for the sensor placement due to confined space. They had to be positioned in quadrature within the interference pattern. At the same time, it had to be made sure that the CO_2 laser beam could not melt any optomechanical components. Another was that once the fiber was heated, the surrounding air also heated up, creating convection around the fiber. This caused the fiber to vibrate and subsequently altered the position of the interference pattern distorting the measured data. To counteract this effect, the length of fiber sus-
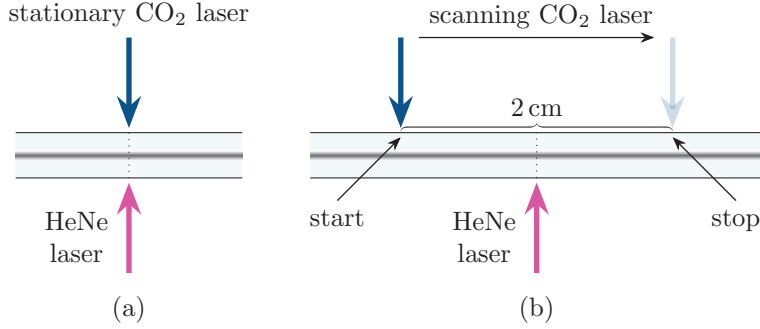
Figure 5.4: Illustration of the fixed measurement point (dotted line) for (a) the stationary case with a fixed CO_2 laser exposure point and (b) the scanning case with a scanning CO_2 laser beam.

pended freely in air was kept as short as possible, while making sure that the fiber, when heated at the starting point, did not warm up at the temperature measurement point (compare Fig. 5.4(b)). Last, the fiber tended to deform, especially at the highest laser powers at which the silicon core was molten. A good ratio of power and annealing speed had to be found at which the core is already molten, but the fiber does not deform yet. Nonetheless, it was possible to measure the temperature in the stationary case and for scanning speeds ranging from $v = 0.1\,\mathrm{mm\,s^{-1}}$ to $v = 10\,\mathrm{mm\,s^{-1}}$. In each case, the temperature was measured at four different laser powers between $P = 5.8\,\mathrm{W}$ and $P = 35.9\,\mathrm{W}$.

The measured temperature profile for the stationary case is shown in Figure 5.5(a) for a laser power of $P = 23.0\,\mathrm{W}$. In this case, the fiber was heated respectively cooled instantaneously by opening and closing a shutter. A quick temperature rise was measured upon opening the shutter at $t = 1\,\mathrm{s}$. Closing the shutter at $t = 5\,\mathrm{s}$ led to a rapid decrease in temperature. Further, it can be seen that heating was faster than cooling. Figures 5.5(b) to (d) show the measured temperature profiles for the same laser power, $P = 23.0\,\mathrm{W}$, as in the stationary case but for different scanning speeds. It is noticeable that the maximum temperature decreased with increasing velocity. Further, the shape of the temperature profile appears almost symmetrical on the cooling and the heating side for a slow scanning speed of $1\,\mathrm{mm\,s^{-1}}$. The
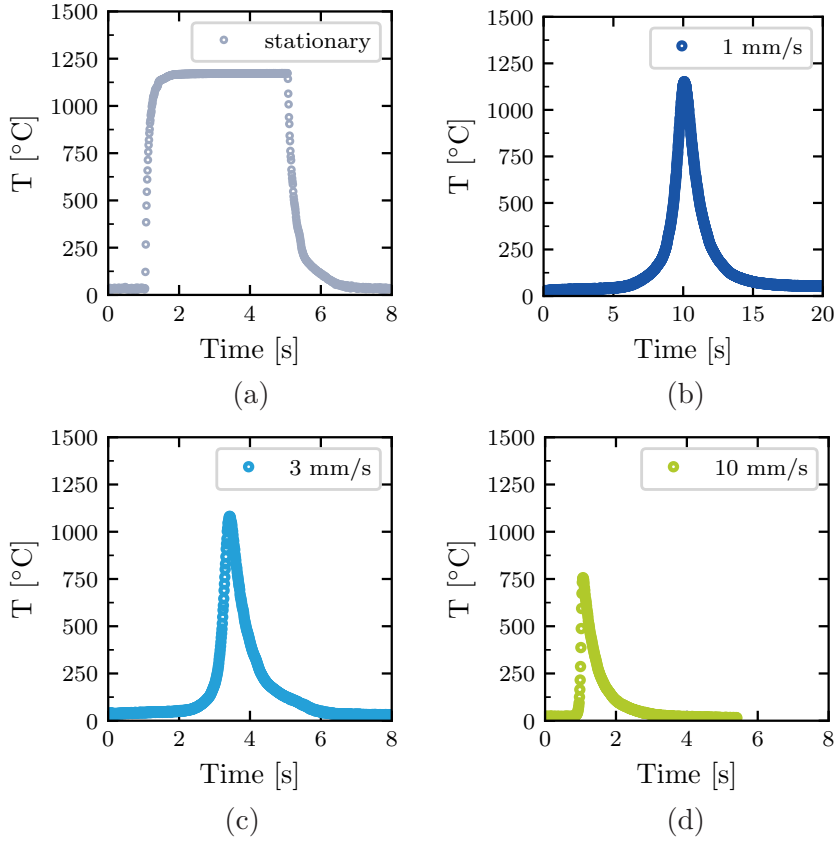
Figure 5.5: Comparison of the measured temperature profiles for a $125\,\mu m$ SCF with a $20\,\mu m$ silicon core when scanned with different speeds by a CO_2 laser at a power of $P = 23.0\,W$.

profile became less symmetrical for faster scanning speeds. Figure 5.6 illustrates how the different laser powers affected the temperature profile at a scanning speed of $v = 3\,mm\,s^{-1}$. It can be seen that the temperature rose quickly when the CO_2 laser beam approached the measurement point, and that cooling of the SCF was slower than heating. The shape of the profile is similar for all laser powers, while the maximum temperature increased for higher laser powers.

A summary of the obtained maximum temperatures for all performed measurements is given in Fig. 5.7. It becomes apparent that
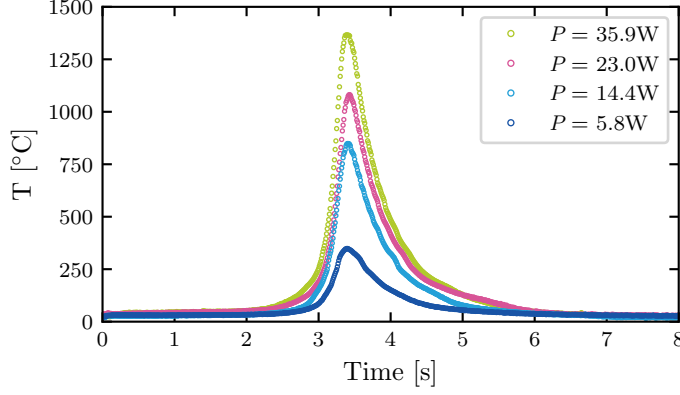
Figure 5.6: Temperature profile for a 125 μm SCF with a 20 μm silicon core showing the effect of different laser powers on temperature dynamics and peak temperature.

slower scanning speeds and higher power led to higher peak temperatures. Faster scanning speeds and lower power led to lower peak temperatures. There are missing data points for the lowest speeds at the highest powers. These were either caused by deformation of the fiber at these high temperatures or convection-induced vibrations of the fiber, which consequently altered the interference pattern. Nonetheless, a maximum temperature of 1367 °C was measured for a laser power of 35.9 W and a scanning speed of $3\,\mathrm{mm\,s^{-1}}$. It is worth noting that the images of the CMOS camera clearly showed a molten silicon core of the fiber for the two scanning speeds $v = 3\,\mathrm{mm\,s^{-1}}$ and $v = 5\,\mathrm{mm\,s^{-1}}$ at the highest set laser power of $P = 35.9\,\mathrm{W}$. The molten silicon core was visible at a measured maximum temperature above 1281 °C, well below the ambient pressure melting point of crystalline silicon at 1414 °C. Lower laser powers heated the SCF up to 1173 °C and were insufficient to melt the silicon core at any of the investigated scanning speeds.

Additionally, the cooling rates were determined from the temperature profiles by fitting an exponential function to the cooling side. The cooling rate was defined as

$$\frac{dT}{dt} = \frac{T_{\mathrm{MAX}} - T_{1/e}}{\tau}, \tag{5.1}$$
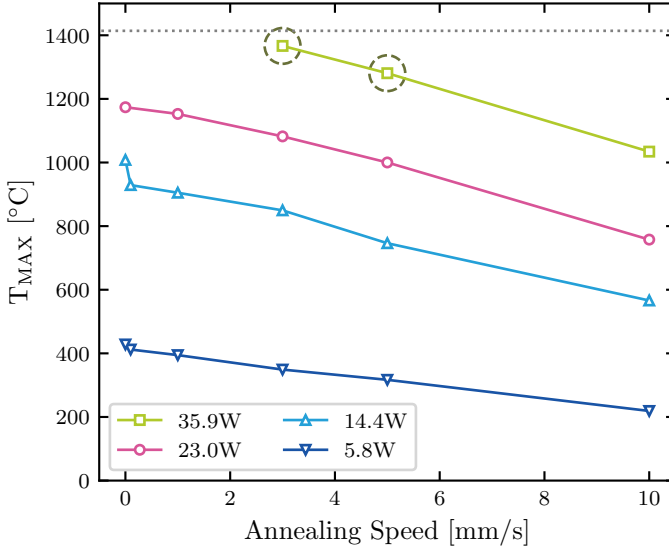
Figure 5.7: Maximum measured temperatures for a SCF depending on scanning speed and laser power. The measurement points highlighted by dashed circles correspond to those with a molten silicon core. The grey dotted line indicates the ambient melting point of silicon at $T = 1414\,°C$.

where T_{MAX} is the maximum temperature, $T_{1/e} = T_{MAX}/e$ and τ is the time constant obtained from the exponential fit. The resultant cooling rates are shown in Fig. 5.8. The plot illustrates that higher peak temperatures and faster scanning speeds led to higher cooling rates. In the stationary case, the heating power was taken away from the fiber almost instantaneously by closing the shutter. This led to the highest measured cooling rate of $3504\,°C\,s^{-1}$. The highest cooling rate measured in the scanning case was $2003\,°C\,s^{-1}$ for a velocity of $5\,mm\,s^{-1}$. Likely, the cooling rate would be even higher for scanning at $10\,mm\,s^{-1}$ if the same maximum temperatures were to be reached without fiber deformation.

Looking closer at the temperature profiles during annealing (see Fig. 5.5 and Fig. 5.6), their shape can be explained by considering the heating and cooling mechanisms acting on the SCF. On the one hand, heat was provided through the CO_2 laser beam. The
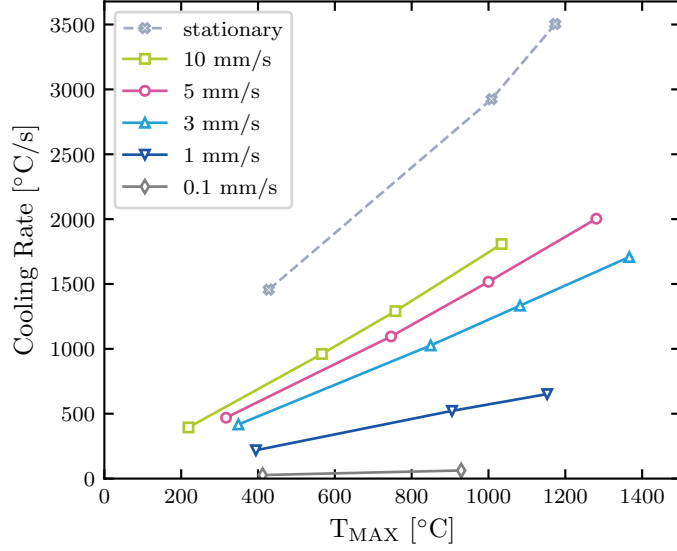
Figure 5.8: Cooling rates of the SCF for the stationary (dashed line) and the scanning case (solid lines).

amount of deposited heat was set by the laser power and the scanning speed, which changed the heating time of each fiber section. On the other hand, heat was removed from the fiber only by natural cooling mechanisms: convection, conduction, and radiation. The resulting implications are discussed in more detail in **Paper V**. Here, the focus of the discussion is on two points. One is the observation that for the fastest investigated scanning speed, the measured cooling rates were slower than the experimentally determined natural cooling rates of the stationary case. This implies a potential for further reduction of transmission losses of SCFs by approaching the cooling rate of the stationary case either in postprocessing or already during fiber manufacturing. The other is the surprisingly low temperature (1281 °C) at which a molten silicon core was observed. The difference to the bulk melting point of silicon at 1414 °C might partly be explainable by the error in the temperature measurement of ±35.6 °C as discussed in Section 2.4. However, that would still leave a discrepancy of ≈ 100 °C unexplained. This discrepancy in melting temperature could be attributed to inbuilt stress in the fiber.

In the case of the SCF investigated here, this stress arises during the fabrication in the fiber draw tower (see Section 4.2, Ref. [20]) during which a preform is heated above the silicon melting point. The glass cladding is softened and acts as a crucible. The fiber leaves the draw tower furnace, cools down, and the core solidifies. In this scenario, two effects compete and cause the final stress distribution in the SCF. One is that silicon expands by $\approx 9\%$ when solidifying. Axially, the melt zone can compensate for this rapid expansion. Radially, the glass cladding can only accommodate a certain amount leaving residual radial compressive stress. The second is the different thermal expansion coefficients of the silicon core ($\approx 2.6\,\text{K}^{-1}$) and the silica cladding ($\approx 0.6\,\text{K}^{-1}$) [3, 38]. When the fiber cools down to room temperature, the radial compressive stress will decrease, and axial tensile stress will rise. This tensile stress at room temperature can be seen using Raman spectroscopy. It caused the downshift of the Raman peak for silicon shown in Fig. 5.9. However, this Raman spectrum does
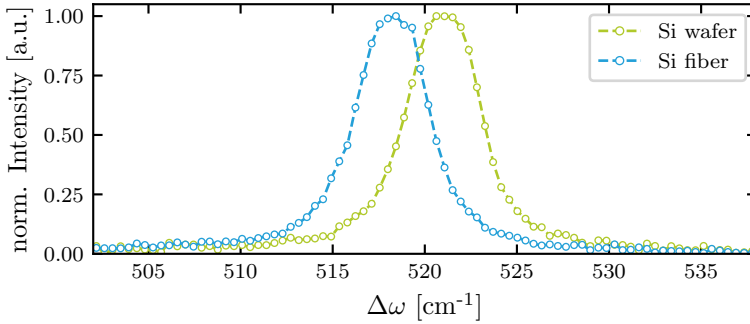
Figure 5.9: Raman spectra of a silicon wafer (green) and the investigated SCF (blue).

not give information about the stress at higher temperatures at which the presented experiments were conducted. Increased temperatures will lower the axial tensile stress, which is expected to disappear at the melting point. But, the radial compressive stress increases with increasing temperature. This compressive stress is believed to cause the lowered melting point of the silicon core at $1281\,°\text{C}$. The measured melting point indicates a compressive stress of $\approx 2\,\text{GPa}$ following the T-P phase diagram of bulk silicon given in Ref. [58].

6 Conclusion

The research within the scope of this thesis was focused on developing a temperature measurement technique for SCFs during laser-based processing in a specially developed processing setup. While most of the scientific findings are demonstrated and discussed in the appended papers, the focus of the preceding chapters was on framing the papers into a conclusive story, giving technical background information, and highlighting the main findings of the temperature measurements in SCFs during CO_2 laser processing.

In this thesis work, an advanced laser processing system was developed. This system was used for the fiber processing presented in Ref. [59]. It was optimized and stabilized for the induction of a constant temperature in fused silica employing a specially developed feedback system. For this feedback system, a specialized controller was developed [60] that was extended into a fully computer-controlled command central, which in addition to controlling the laser power itself synchronized all additional measurement equipment used in the various experiments. Calibration of the feedback system was conducted, allowing for in-situ non-contact temperature measurements in optical fibers up to the glass softening point [45]. This feedback system exploits the circular cross-section of a fiber as a Fabry-Pérot cavity. This technique was then modified to allow for temperature measurements in optical fibers with an opaque core such as SCFs by probing the fiber in a Mach-Zehnder-type configuration [37]. Before SCFs could be processed, they needed to be manufactured, for which purpose a fiber draw tower was developed. Here, the software interface for the CO_2 laser controller has proven to be a solid foundation for the draw tower control software. The developed tower was mainly used for the production of SCFs and demonstrated to deliver fibers with relatively low losses of $0.2\,\mathrm{dB\,cm^{-1}}$ in the near infrared [20].

Finally, the developed temperature measurement technique could be used to monitor fabricated SCFs during subsequent CO_2 laser processing in the specially designed fiber processing setup. The main results are presented in Ref. [59]. For the first time, to the best of my knowledge, this direct temperature measurement of a silicon core fiber during CO_2 laser annealing has been demonstrated. It was possible to measure temperatures up to $T = 1367\,°\mathrm{C}$ only limited by the softening of the fiber. It was also found that the silicon core of the fiber was already molten at this temperature and even at a lower temperature of $1281\,°\mathrm{C}$. This was attributed to the compressive stress in the fiber. However, more analysis needs to be done in the future to confirm the calculated stress of $\approx 2\,\mathrm{GPa}$. Additionally, cooling rates as high as $\approx 3500\,°\mathrm{C\,s^{-1}}$ were determined from the measured temperature profiles in the case of instantaneous heating and cooling while for annealing the measured cooling rates did not exceed $\approx 2000\,°\mathrm{C\,s^{-1}}$. This study proved the temperature measurement technique to be a viable means of in-situ temperature monitoring during semiconductor core fiber fabrication and postprocessing and helped in understanding that the optical transmission losses in those fibers can be further reduced by faster draw or processing speeds.

References

[1] K. C. Kao and G. A. Hockham, "Dielectric-fibre surface waveguides for optical frequencies", *Proceedings of the Institution of Electrical Engineers* **113**, 1151–1158 (1966).

[2] G. F. Taylor, "A method of drawing metallic filaments and a discussion of their properties and uses", *Physical Review* **23**, 655–660 (1924).

[3] P. J. A. Sazio et al., "Microstructured optical fibers as high-pressure microfluidic reactors", *Science* **311**, 1583–1586 (2006).

[4] D. A. Coucheron et al., "Laser recrystallization and inscription of compositional microstructures in crystalline SiGe-core fibres", *Nature Communications* **7**, 13265 (2016).

[5] W. G. Pfann, "Zone melting", *Metallurgical Reviews* **2**, 29–76 (1957).

[6] R. Kitamura, L. Pilon, and M. Jonasz, "Optical constants of silica glass from extreme ultraviolet to far infrared at near room temperature", *Applied Optics* **46**, 8118–8133 (2007).

[7] B. Temelkuran et al., "Wavelength-scalable hollow optical fibres with large photonic bandgaps for CO_2 laser transmission", *Nature* **420**, 650–653 (2002).

[8] J. S. Sanghera and I. D. Aggarwal, "Active and passive chalcogenide glass optical fibers for IR applications: a review", *Journal of Non-Crystalline Solids* **256-257**, 6–16 (1999).

[9] V. S. Shiryaev and M. F. Churbanov, "Recent advances in preparation of high-purity chalcogenide glasses for mid-IR photonics", *Journal of Non-Crystalline Solids* **475**, 1–9 (2017).

[10] M. Ordu and S. N. Basu, "Recent progress in germanium-core optical fibers for mid-infrared optics", *Infrared Physics and Technology* **111**, 103507 (2020).

[11] J. R. Sparks et al., "Zinc selenide optical fibers", *Advanced Materials* **23**, 1647–1651 (2011).

[12] T. Sørgård et al., "Broadband infrared and THz transmitting silicon core optical fiber", *Optical Materials Express* **10**, 2491–2499 (2020).

[13] H. Ren et al., "Low-loss silicon core fibre platform for mid-infrared nonlinear photonics", *Light: Science and Applications* **8**, 105 (2019).

[14] L. Shen et al., "A review of nonlinear applications in silicon optical fibers from telecom wavelengths into the mid-infrared spectral region", *Optics Communications* **463**, 125437 (2020).

[15] A. C. Peacock and N. Healy, "Semiconductor optical fibres for infrared applications: a review", *Semiconductor Science and Technology* **31**, 103004 (2016).

[16] D. Homa et al., "Silicon fiber with p-n junction", *Applied Physics Letters* **105**, 122110 (2014).

[17] F. A. Martinsen et al., "Silicon-core glass fibres as microwire radial-junction solar cells", *Scientific Reports* **4**, 6283 (2014).

[18] J. R. Sparks, P. J. Sazio, V. Gopalan, and J. V. Badding, "Templated chemically deposited semiconductor optical fiber materials", *Annual Review of Materials Research* **43**, 527–557 (2013).

[19] U. J. Gibson, L. Wei, and J. Ballato, "Semiconductor core fibres: materials science in a bottle", *Nature Communications* **12**, 3990 (2021).

[20] C. M. Harvey et al., "Specialty optical fiber fabrication: fiber draw tower based on a CO laser furnace", *Journal of the Optical Society of America B* **38**, F122–F129 (2021).

[21] J. Ballato et al., "Silicon optical fiber", *Optics Express* **16**, 18675–18683 (2008).

[22] H. Ren et al., "Tapered silicon core fibers with nano-spikes for optical coupling via spliced silica fibers", *Optics Express* **25**, 24157 (2017).

[23] E. F. Nordstrand, A. N. Dibbs, A. J. Eraker, and U. J. Gibson, "Alkaline oxide interface modifiers for silicon fiber production", *Optical Materials Express* **3**, 651–657 (2013).

[24] A. C. Peacock, U. J. Gibson, and J. Ballato, "Silicon optical fibres – past, present, and future", *Advances in Physics: X* **1**, 114–127 (2016).

[25] X. Ji et al., "Single-crystal silicon optical fiber by direct laser crystallization", *ACS Photonics* **4**, 85–92 (2017).

[26] N. Healy et al., "CO_2 laser-induced directional recrystallization to produce single crystal silicon-core optical fibers with low loss", *Advanced Optical Materials* **4**, 1004–1008 (2016).

[27] M. Kudinova et al., "Two-step manufacturing of hundreds of meter-long silicon micrometer-size core optical fibers with less than 0.2 dB/cm background losses", *APL Photonics* **6**, 026101 (2021).

[28] Y. Zou et al., "Mid-infrared silicon photonic waveguides and devices [Invited]", *Photonics Research* **6**, 254–276 (2018).

[29] J. Degallaix et al., "Bulk optical absorption of high resistivity silicon at 1550 nm", *Optics Letters* **38**, 2047–2049 (2013).

[30] F. P. Kapron, D. B. Keck, and R. D. Maurer, "Radiation losses in glass optical waveguides", *Applied Physics Letters* **17**, 423 (1970).

[31] P. Debije, "Das elektromagnetische Feld um einen Zylinder und die Theorie des Regenbogens", *Physikalische Zeitschrift* **9**, 775–778 (1908).

[32] E. Hecht, *Optics*, 5th ed. (Pearson Education, 2017).

[33] J. Wang and J. L. Pressesky, "Quadrature phase shift interferometer (QPSI) decoding algorithms and error analysis", *Proc. SPIE* **5188**, 71–79 (2003).

[34] H. Gao et al., "Investigation on the thermo-optic coefficient of silica fiber within a wide temperature range", *Journal of Lightwave Technology* **36**, 5881–5886 (2018).

[35] M. Fokine, "Formation of thermally stable chemical composition gratings in optical fibers", *Journal of the Optical Society of America B* **19**, 1759–1765 (2002).

[36] M. Fokine, "Growth dynamics of chemical composition gratings in fluorine-doped silica optical fibers", *Optics Letters* **27**, 1974–1976 (2002).

[37] C. M. Harvey, K. Mühlberger, and M. Fokine, "Mach-Zehnder interferometer for in-situ non-contact temperature monitoring during thermal processing of an optical fibre", *Journal of Lightwave Technology* **39**, 7223–7230 (2021).

[38] M. Fokine et al., "Laser structuring, stress modification and Bragg grating inscription in silicon-core glass fibers", *Optical Materials Express* **7**, 1589–1597 (2017).

[39] R. A. Logan and W. L. Bond, "Density change in silicon upon melting", *Journal of Applied Physics* **30**, 322 (1959).

[40] H. S. Nalwa, *Silicon-based material and devices*, 1st ed. (Academic Press, 2001).

[41] C. K. Patel, "Continuous-wave laser action on vibrational-rotational transitions of CO_2", *Physical Review* **136**, A1187–A1193 (1964).

[42] C. K. Patel, "Interpretation of CO_2 optical maser experiments", *Physical Review Letters* **12**, 588–590 (1964).

[43] O. Svelto, *Principles of Lasers*, 5. ed. (Springer, 2010).

[44] W. Demtröder, *Atoms, Molecules and Photons: An Introduction to Atomic-, Molecular- and Quantum Physics*, 3rd ed. (Springer, 2018).

[45] K. Mühlberger, C. M. Harvey, and M. Fokine, "In-situ non-contact high-temperature measurement of an optical fiber up to the glass softening point", *Optics Express* **29**, 7825–7832 (2021).

[46] S. R. Nagel, J. B. MacChesney, and K. L. Walker, "An overview of the modified chemical vapor deposition (MCVD) process and performance", *IEEE Transactions on Microwave Theory and Techniques* **30**, 305–322 (1982).

[47] J. Ballato and P. Dragic, "Rethinking optical fiber: new demands, old glasses", *Journal of the American Ceramic Society* **96**, 2675–2692 (2013).

[48] T. Oriekhov, C. M. Harvey, K. Mühlberger, and M. Fokine, "Specialty optical fiber fabrication: preform manufacturing based on asymmetrical CO Laser heating", *Journal of the Optical Society of America B* **38**, F130–F137 (2021).

[49] U. C. Paek, "Laser drawing of optical fibers", *Applied Optics* **13**, 1383–1386 (1974).

[50] A. Heptonstall et al., "Invited Article: CO_2 laser production of fused silica fibers for use in interferometric gravitational wave detector mirror suspensions", *Review of Scientific Instruments* **82**, 011301 (2011).

[51] A. D. McLachlan and F. P. Meyer, "Temperature dependence of the extinction coefficient of fused silica for CO_2 laser wavelengths", *Applied Optics* **26**, 1728–1731 (1987).

[52] S. Uma et al., "Temperature-dependent thermal conductivity of undoped polycrystalline silicon layers", *International Journal of Thermophysics* **22**, 605–616 (2001).

[53] S. Elhadj et al., "Determination of the intrinsic temperature dependent thermal conductivity from analysis of surface temperature of laser irradiated materials", *Applied Physics Letters* **96**, 071110 (2010).

[54] T. Satō, "Spectral Emissivity of Silicon", *Japanese Journal of Applied Physics* **6**, 339–347 (1967).

[55] E. Takasuka, E. Tokizaki, K. Terashima, and S. Kimura, "Emissivity of liquid silicon in visible and infrared regions", *Journal of Applied Physics* **81**, 6384–6389 (1997).

[56] T. Sørgård et al., "All-optical high-speed modulation of THz transmission through silicon core optical fibers", *Optics Express* **29**, 3543–3552 (2021).

[57] S. Song et al., "Laser restructuring and photoluminescence of glass-clad GaSb/Si-core optical fibres", *Nature Communications* **10**, 1790 (2019).

[58] C. C. Yang, J. C. Li, and Q. Jiang, "Temperature-pressure phase diagram of silicon determined by Clapeyron equation", *Solid State Communications* **129**, 437–441 (2004).

[59] K. Mühlberger, C. M. Harvey, and M. Fokine, "Temperature dynamics in silicon core fibers during CO_2 laser processing", *Optics Express* **30**, 92–100 (2022).

[60] K. Mühlberger, C. M. Harvey, and M. Fokine, "High-performance arduino-based interferometric quadrature phase-shift detection system with 1 nm resolution", *AIP Advances* **11**, 105304 (2021).